RSC Advances

PAPER

Cite this: *RSC Adv.*, 2025, **15**, 15318

Development of bixbyite microdice fabricated cathode for aqueous rechargeable zinc ion batteries†

Nusrat Tazeen Tonu, [ab] Mohammad Abu Yousuf, *[a] Parbhej Ahamed [a] and Md. Mahfujul Hasan[c]

In this study, an ultrasonic-aided reverse micelle formation, followed by the calcination route, was developed for the synthesis of bixbyite microdice aimed at the fabrication of a cathode for ARZIBs. The prepared product was Mn_2O_3 having crystallinity and grain size of 65.12% and 25.61 nm, respectively, with a small percentage of other Mn-based oxides within it. The FESEM image showed dice like microsized Mn_2O_3, revealing the possible formation of a reverse micelle core of approximately 500 nm. XPS narrow spectra revealed the presence of Mn^{3+} in a mixture of Mn with +2 and +4 oxidation states. The crystal planes from the TEM images matched with XRD results and strengthened the formation of bixbyite Mn_2O_3 nanoparticles. The optical band gap of 3.21 eV specified the semiconducting property of the prepared Mn_2O_3, and therefore, the prepared Mn_2O_3 was used as a cathode material in a CR-2032 coin cell of ARZIBs. CV showed a reversible reaction within the cell, indicating the (de)intercalation of Zn^{2+} ions between the anode and cathode. The fresh cell showed high conductivity and low resistance compared with the used cell after BCD testing, confirmed by EIS. The cell delivered high specific discharge capacities of 293.59 ± 4.75 and 252.10 ± 4.66 mA h g^{-1} at applied current densities of 0.1 and 0.3 A g^{-1}, respectively. Consequently, BCD was performed for 1000 cycles at a current density of 0.3 A g^{-1}. Throughout the cycling, the capacity retention and coulombic efficiency were maintained at 90.35 ± 0.30% and 98.44 ± 0.27%, respectively, suggesting the resilient reversibility of charging and discharging.

Received 23rd January 2025
Accepted 28th April 2025

DOI: 10.1039/d5ra00543d

rsc.li/rsc-advances

1. Introduction

The environment and its energy systems are essential for human survival and prosperity. Since natural resources are finite, fossil fuel usage and energy demand have increased worldwide interest in energy technologies. Moreover, since smartphones, computers, electronic automobiles, *etc.* are so popular, rechargeable batteries are in demand.[1,2] In recent decades, rechargeable batteries such as lead-acid (LABs), Li^+-ion (LIBs), Na^+-ion, and Zn^{2+}-ion (ZIBs) batteries have been developed.[3] Among the oldest and most popular rechargeable batteries are LABs. However, Pb toxicity, limited energy density, and deep discharge with overcharging restrict LABs.[4,5] Unlike LABs, LIBs are the most popular rechargeable batteries for electrical and electronic vehicles owing to their extended lifespan, high voltage, and high energy density. Unfortunately, volatile organic electrolytes and the scarcity and flammability of Li make LIBs unfeasible.[6,7] LIBs pose a major threat to those who dominate the current energy market; thus, the development of new batteries is imminent.[8]

Aqueous rechargeable batteries appear promising over LIBs for two reasons. First, organic electrolytes are replaced with aqueous ones to avoid fires, reducing short circuit costs. Second, water's stronger ionic conductivity than organic solvents' allows higher battery operation.[9] Meanwhile, aqueous rechargeable zinc ion batteries (ARZIBs) are gaining popularity because of their environmental friendliness, safety, availability, affordability (US$2.4 kg^{-1}), high theoretical capacities (820 mA h g^{-1} and 5855 mA h cm^{-3}), low potential, and suitable Zn^{2+}|Zn reduction potential (−0.76 V *vs.* SHE).[10] Zn-based aqueous batteries were first fabricated in the 1980s. Zn-air and Zn–MnO_2 batteries use alkaline media for charge–discharge electrochemistry. Zinc dendrite development and aqueous electrolyte-induced side reaction have delayed water-based ZIB commercialization.[11] Electrostatic repulsions between host materials and divalent Zn^{2+} ions make ARZIB cathode materials difficult to find. Prussian blue analogues, V-based cathodes have been developed. However, Mn-based cathodes provide better electrochemical storage performance compared with Zn^{2+}|Zn potential, and are a suitable voltage platform (1.25 V).[12,13]

[a]*Department of Chemistry, Khulna University of Engineering and Technology, Khulna, 9203, Bangladesh. E-mail: yousuf@chem.kuet.ac.bd; nusrattazeen@ku.ac.bd; parbhej@chem.kuet.ac.bd*

[b]*Chemistry Discipline, Khulna University, Khulna, 9208, Bangladesh*

[c]*Food and Toxicology Research Section, IFST, BCSIR, Dhaka, Bangladesh. E-mail: raihanacce@gmail.com*

† Electronic supplementary information (ESI) available. See DOI: https://doi.org/10.1039/d5ra00543d

At present, a variety of Mn-based oxides has been verified for the Zn^{2+} ion storage in ARZIBs, including α-MnO_2, β-MnO_2, γ-MnO_2, δ-MnO_2, Ω-MnO_2, λ-MnO_2, ε-MnO_2, Mn_2O_3, Mn_3O_4, $ZnMn_2O_4$, *etc.*, consisting of the same fundamental structure of MnO_6, but are linked differently.[14] Among these, MnO_2 is the most explored cathode, but it has weak electrical and ionic conductivities. Besides, it is temperature sensitive, and undergoes a phase transformation to other Mn-oxide above 200 °C.[15] While charging, H^+ ions intercalate to the cathode, competing with Zn^{2+} and leading to sluggish diffusion of Zn^{2+} ion within MnO_2.[16] These simultaneous acts of structural deformation and indolent Zn^{2+} ion diffusion makes MnO_2 problematic for ARZIB. Therefore, Mn_2O_3 has received a lot of focus lately for its easy preparation process, high energy intensity,[17] and high thermal stability up to 850 °C,[18] although they are barely reported for ARZIBs.

A variety of efforts has been made to stabilize and enrich Mn_2O_3 for the storage of Zn^{2+} ion in aqueous media, *e.g.*, preparation process optimization, surface alteration, *etc.* A sacrificial template-based thermal decomposition approach was utilized to create Mn_2O_3, which had a specific discharge capacity of 225.0 and 92.7 mA h g^{-1} at 0.05 and 2.0 A g^{-1}, respectively, and retained its initial discharge capacity after 1700 cycles.[19] Mn_2O_3 was doped with Ni to triple its specific capacity (252 mA h g^{-1} at 0.1 A g^{-1}), and it retained its capacity to 85.6% after 2500 cycles.[20] Precipitation followed by calcination was used to synthesize Mn_2O_3 nanopowder, which showed a specific discharge capacity of 211 mA h g^{-1} at 0.5 A g^{-1} after 200 cycles, and it retained 70% of its initial capacity after 1100 cycles at 2.0 A g^{-1}.[21] Since porosity increases ionic conductivity, porous 3D polymer polypyrrole (PPy)-coated Mn_2O_3 microspheres were developed by applying hydrothermal treatment followed by calcination and polymerization with a conductive PPy, which provided 287.7 mA h g^{-1} at 1.0 A g^{-1} over 300 cycles.[22] Porosity in semiconductors creates additional ion transport pathways. Due to larger linked pores in Mn_2O_3, electron/ion conduction is faster. For smaller surface area and porosity, commercial Mn_2O_3 has poor Zn^{2+} ion capacity. Altering its preparation technique might boost this capacity.[20]

When ultrasound is introduced in a reaction system, it enhances the solubility of reactants with the media, creates heat to enhance mass transport in the system, and produces a vibration which could create cavities or pores within the product, which accelerates the reaction rate.[23] Previously, ultrasound was used to increase the porosity of polyurethane foam.[24] It was also used for homogeneous distribution of nano-SiO_2 within plastomer matrix, and the resultant nano-SiO_2 had a smaller size.[25] Ultrasound was employed to hasten the distribution of Se particles in the hyperbranched polysaccharide dispersion and the size of Se nanoparticle decreased from 100 to 50 nm on average.[26]

$MnCl_2$ and $(NH_4)_2CO_3$ were used as raw materials to prepare nano-sized $MnCO_3$, which is a well-known substitution reaction,[27] followed by the calcination route to prepare Mn_2O_3.[28] However, there are limitations to control the size and shape. In this study, a high frequency ultrasonic assisted novel reverse micelle route was adopted using $MnCl_2$ and $(NH_4)_2CO_3$ to prepare bixbyite Mn_2O_3 microdice where size, shape and porosity have been tuned successfully, which was characterized by physico-chemical and spectroscopic techniques, and applied as cathode material in Zn-ion batteries for electrochemical applications which hasn't been done so far.

2. Materials and methods

2.1 Chemicals and instruments

Manganese(II) chloride tetrahydrate, $MnCl_2 \cdot 4H_2O$ and ammonium carbonate, $(NH_4)_2CO_3$ were purchased from Loba Chemie, India. Cyclohexane (C_6H_{12}), cyclohexanol ($C_6H_{12}OH$) and Triton X-100 were purchased from PT. Smart Lab Indonesia. Zinc sulphate heptahydrate, ($ZnSO_4 \cdot 7H_2O$) was obtained from Sigma-Aldrich (USA). Polyvinylidene fluoride (PVDF), carbon black (C-black), *N*-methyl pyrrolidone, zinc foil, and stainless steel (SS) foil (304 grades) having thickness *t*-0.01 × *w*-100 mm were used for CR-2032 coin cell battery fabrication. All of the work was done using deionized (DI) water. For ultrasonic irradiation, ultrasonic bath (Powersonic 603) was used. To identify the functional groups in the prepared sample, Fourier transform infra-red spectroscopy (FTIR) experiments were done using a FTIR spectrometer (IR Tracer-100, Shimadzu Corporation, Japan). The structure and surface morphology and elemental mapping of the prepared material was analyzed by a field emission scanning electron microscope (FESEM, JSM-7610F, Japan). A small amount of sample was taken for gold coating, then analyzed by the FESEM. Powder X-ray diffractometer (XRD: Bruker, D2PHASER) was used to analyze X-ray diffraction (XRD) of the prepared material with a Cu-Kα radiation source at 2θ from 10° to 80°. A Raman spectroscopic study was performed with a DXR smart Raman spectrometer (Thermo Fisher Scientific Co., Ltd., USA) with an excitation wavelength of 780 nm and full range grating. The elemental composition and valency state of Mn were analyzed by X-ray photoelectron spectroscopy (XPS) (XPS; L-Alpha, Thermo Scientific, UK). The prepared materials shape and crystal planes were evaluated using transmission electron microscopy (TEM) (JEM 2100 PLUS, JEOL, Japan). A small amount of prepared material was taken in a sample vial containing ethanol and shaken well. After that, the vial was enclosed by a cork and sonicated until the particles of the materials were resuspended. The vial was kept at rest for 24 h. A drop of the sample was placed onto a copper grid in a vacuum chamber overnight for degassing. Then, the copper grid containing the sample was analyzed by a TEM analyzer. Solid state UV visible spectroscopy was applied to find out the optical band gap and recorded within the range of 300–800 nm using a UV-1800 spectrophotometer (Shimadzu Corporation, Japan). Cyclic voltammetry (CV), electrochemical impedance spectroscopy (EIS) and battery charging–discharging (BCD) experiments were carried out using a Biologic potentiostat (SP-300).

2.2 Preparation of Mn_2O_3 *via* an ultrasonic assisted reverse micelle route

Cyclohexane : Triton X-100 : cyclohexanol : water (5 : 3 : 2 : 1) was added into a beaker and mixed using an ultrasonic bath at room temperature until a clear mixture was formed, indicating the formation of a microemulsion. The microemulsion was divided

equally into two beakers (B-1 and B-2). 0.005 mole of $MnCl_2$ and $(NH_4)_2CO_3$ were added to B-1 and B-2, respectively and they were kept in an ultrasonic bath until the materials were completely dissolved. Then, the mixture from B-2 was added dropwise into B-1. As the process started with a cloudy appearance, this indicated the production of $MnCO_3$. Ultrasonication was continued for 30 min and all the $MnCl_2$ and $(NH_4)_2CO_3$ were reacted to form $MnCO_3$, which was sedimented as the reaction ended. Then, the product was filtered, air dried and calcined at 400 °C for 3 h. The product was cooled to room temperature and black colored Mn_2O_3 was formed.[29,30] A similar experiment was also carried out using magnetic stirring instead of ultrasonic irradiation. It took longer to produce $MnCO_3$ by magnetic stirring and the amount of product was 61.06% less compared with ultrasonic irradiation. Fig. 1 shows the schematic diagram for the preparation of Mn_2O_3.

2.3 Fabrication of CR-2032 coin cell

Here, the active material is prepared Mn_2O_3, and C-black was used to increase the conductivity of Mn_2O_3, while PVDF was used as the gluing agent and NMP was the solvent; together PVDF and NMP were used as the binding agent. Mn_2O_3, C-black and PVDF were mixed in an 8 : 1 : 1 ratio, followed by the addition of NMP. They were further mixed using a manual mortar and pestle until a smooth slurry was formed. Then, the slurry was applied on a stainless steel foil to form a thin layer.[31] Thereafter, the foil was dried at 70 °C and cut using a die cutting machine which was the final cathode of the battery. The fabrication of the CR-2032 coin cell of ARZIB was done through the arrangement of cathode metal case, fabricated cathode, separator soaked with aqueous 2.0 M $ZnSO_4$ as electrolyte, Zn foil as the anode, with a spacer, spring, and anode metal case.[32] About 20 batteries were made for electrochemical testing.

3. Results and discussion

Fig. 2 shows the FTIR spectra of the prepared products between a wavenumber range of 400 to 4000 cm^{-1}. The peak positions

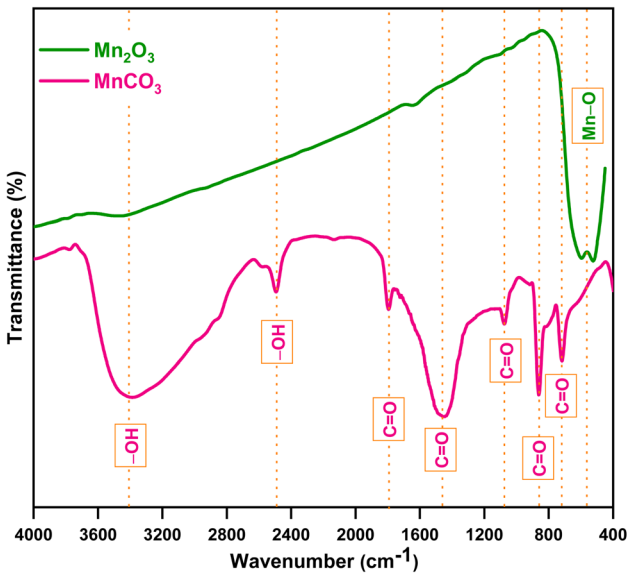

Fig. 2 FTIR spectrum of the prepared products.

were also labelled with dotted straight lines. For $MnCO_3$, a broad peak with high intensity at 3404 cm^{-1} represents the stretching vibrations of O–H, a sharp peak with low intensity at 2489 cm^{-1} indicates the bending vibration of O–H in H_2O, which is due to moisture in the KBr plate. Sharp peaks with low intensity at 1799 and 1073 cm^{-1}, and high intensity at 1457, 867 and 718 cm^{-1} represented the vibration of C=O in $MnCO_3$. For Mn_2O_3, a broad peak at 566 cm^{-1} represented the Mn–O vibration in MnO_6–octahedral moiety, which indicated the presence of Mn–oxide. These results indicated that the ultrasonic assisted reverse micelle route produced $MnCO_3$ that formed Mn-based oxide after calcination. Furthermore, the line intensity of Mn_2O_3 decreased as the wave number increased, which implies it's crystalline and/or semiconducting behavior.[33,34]

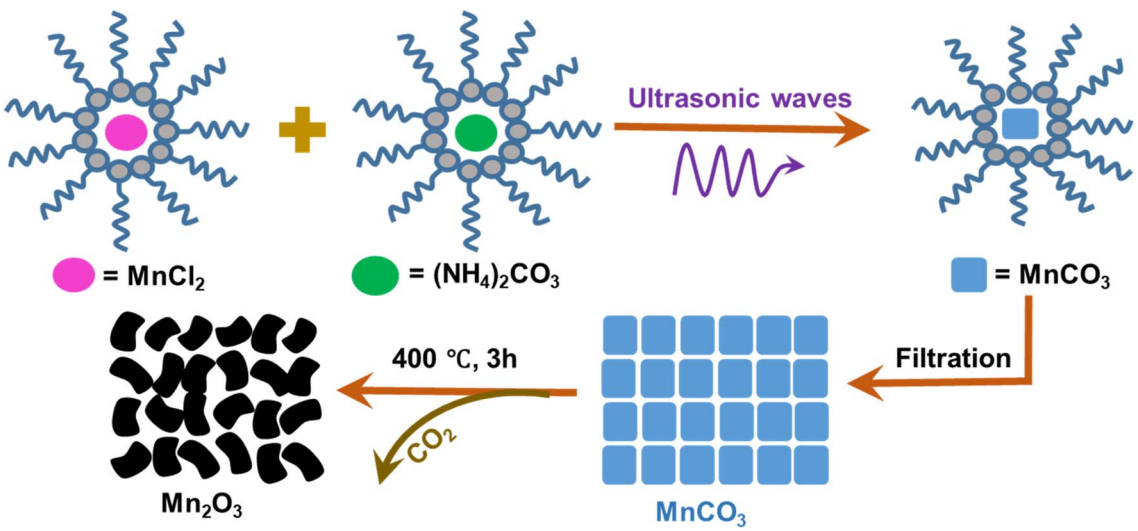

Fig. 1 Synthesis of Mn_2O_3 *via* an ultrasonic assisted reverse micelle route (reaction scheme).

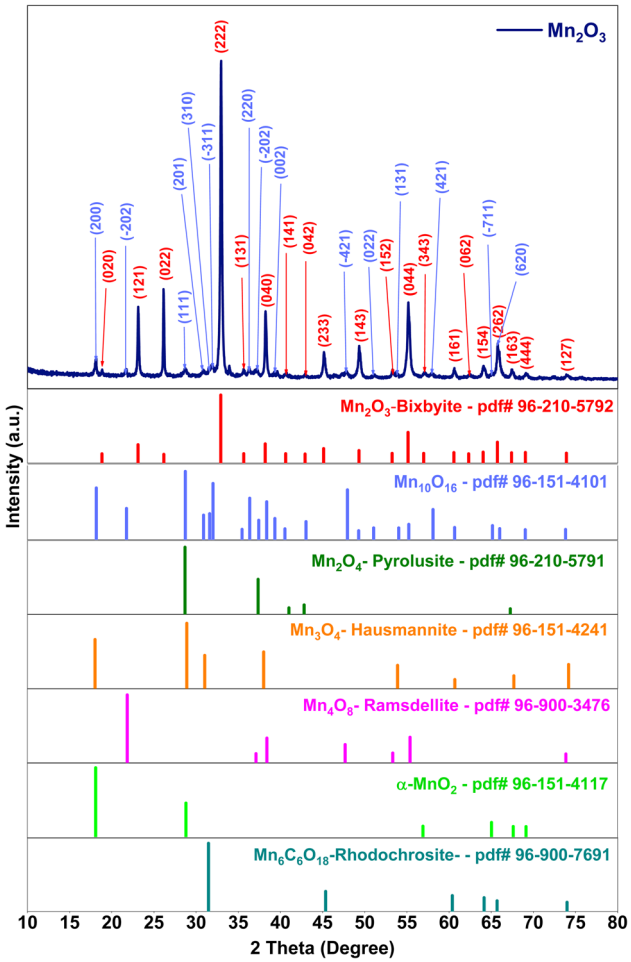

Fig. 3 Powder XRD of the prepared Mn_2O_3 with standard references.

The prepared Mn_2O_3 was subjected to powder XRD analysis to determine the crystalline structure and purity. An X-ray diffractogram of the prepared Mn_2O_3 is shown in Fig. 3. Diffraction peaks were found at 2θ = 18.14°, 18.85°, 21.69°, 23.13°, 26.13°, 28.70°, 30.85°, 31.96°, 32.96°, 33.93°, 35.61°, 36.36°, 37.17°, 38.23°, 39.62°, 40.72°, 42.93°, 45.16°, 47.79°, 49.33°, 51.18°, 53.28°, 53.71°. 55.17°, 57.13°, 57.94°, 60.62°, 62.32°, 64.06°, 65.77°, 66.01°, 67.41°, 69.11°, 73.89°, and 73.91°. This spectrum was analyzed using X'pert Highscore Plus software and a mixture of Mn based oxides were found by matching with the Crystallographic Open Database (COD). The spectrum primarily matched with Mn_2O_3 (77% with bixbyte, COD_Pdf # 96-210-5792), along with Mn_5O_8 (34% with $Mn_{10}O_{16}$, COD_Pdf # 96-151-4101), Mn_2O_4 (18% with pyrolusite, COD_Pdf # 96-210-5791), Mn_3O_4 (13% with hausmannite, COD_Pdf # 96-151-4241), Mn_4O_8 (10% with ramsdellite, COD_Pdf # 96-900-3476), α-MnO_2 (8%, COD_Pdf # 96-151-4117) and $Mn_6C_6O_{18}$ (10% with rhodochrosite, COD_Pdf # 96-900-7691). The suspected planes of the prepared Mn_2O_3 w. r. to 2θ compared with the references are listed in Table 1. Therefore, the prepared Mn-oxide is mainly Mn_2O_3 with a small amount of Mn_5O_8, which also contains a trace amount of MnO_2 and Mn_3O_4; thus, it was being considered as Mn_2O_3. This could be credited to the cubic crystal system of the $I\,a\bar{3}$ space group (no. 206).

The Scherer eqn (1) was used to calculate the average crystal size of prepared Mn_2O_3:

$$D = \frac{K\lambda}{\beta \cos\theta} \quad (1)$$

where D = crystallite size in nm, λ= wavelength of X-ray in nm (0.15406 nm), β = full wave half maxima (FWHM) of the peaks, K = Scherer constant (0.9), and θ = Braggs angle in radians.[35]

Table 1 Peak position of the prepared Mn_2O_3 with respect to crystal planes compared with references

2θ (°)	Planes (h *k* l) compared with Mn_2O_3 (COD_Pdf # 96-210-5792)	2θ (°)	Planes (*h k l*) Compared with Mn_5O_8 (COD_Pdf # 96-151-4101)
18.85	(0 2 0)	18.14	(2 0 0)
23.13	(1 2 1)	21.69	(-2 0 2)
26.13	(0 2 2)	28.70	(1 1 1)
33.93	(2 2 2)	30.85	(2 0 1)
35.61	(1 3 2)	31.96	(3 1 0)
38.23	(0 4 0)	32.96	(-3 1 1)
40.72	(1 4 1)	36.36	(2 2 0)
42.93	(0 4 2)	37.17	(-2 0 2)
45.16	(2 3 3)	39.62	(0 0 2)
49.33	(1 4 3)	47.79	(-4 2 1)
53.28	(1 5 2)	51.18	(0 2 2)
55.17	(0 4 4)	53.71	(1 3 1)
57.13	(3 4 3)	57.94	(4 2 1)
60.62	(1 6 1)	64.62	(-7 1 1)
62.32	(0 6 2)	66.01	(6 2 0)
64.06	(1 5 4)		
65.77	(2 6 2)		
67.41	(1 6 3)		
69.11	(4 4 4)		
73.91	(1 2 7)		

The calculated average crystallite size (D) was 25.61 nm with 65.12% crystallinity.

The d-spacing calculation was done using Bragg's law (2):

$$n\lambda = 2d \sin\theta, \quad \text{or} \quad d = \frac{n\lambda}{2\sin\theta} \tag{2}$$

where λ= wavelength of incident X-ray (1.5406 Å), θ = peak position in radians, $n = 1$ (order of diffraction), $d = d$-spacing or interplanar spacing in Å.

For the cubic cell, the lattice constant was calculated using eqn (3):

$$\frac{1}{d^2} = \frac{h^2 + k^2 + l^2}{a^2} \tag{3}$$

where, $a = b = c$ = lattice constant of unit cell, d = interplanar spacing or d-spacing; h, k, and l = Miller indices. The lattice constants were calculated using the values of d-spacing.[36] The values calculated using eqn (6) and (7) are given in Table 2. The calculated values of lattice parameter $a = b = c = 9.4147$ Å is very close to the standard value (9.4150 Å).[34,37] Other parameters of unit cell volume, micro-strain and dislocation density were also calculated using eqn (4)–(6), respectively.

$$\text{Unit cell volume, } V = a^3 \tag{4}$$

$$\text{Micro-strain, } \varepsilon = \frac{\beta}{4\tan\theta} \tag{5}$$

$$\text{Dislocation density, } \delta = \frac{1}{D^2}\text{lines per nm}^2 \tag{6}$$

Table 2 The calculated values of interplanar spacing with respect to the peak positions and Miller indices of the prepared Mn_2O_3 from the XRD pattern

Peak positions, 2Theta (°)	Interplanar spacing, d (Å)	Miller indices, (h k l)
18.85	4.703938	(0 2 0)
23.13	3.842288	(1 2 1)
26.13	3.407558	(0 2 2)
33.93	2.717783	(2 2 2)
35.61	2.519145	(1 3 2)
38.23	2.352310	(0 4 0)
40.72	2.214030	(1 4 1)
42.93	2.105031	(0 4 2)
45.16	2.006130	(2 3 3)
49.33	1.845861	(1 4 3)
53.28	1.717950	(1 5 2)
55.17	1.663485	(0 4 4)
57.13	1.610982	(3 4 3)
60.62	1.526319	(1 6 1)
62.32	1.488705	(0 6 2)
64.06	1.452401	(1 5 4)
65.77	1.418719	(2 6 2)
67.41	1.388135	(1 6 3)
69.11	1.358082	(4 4 4)
73.91	1.281297	(1 2 7)

where D is the crystallite size in nm. The calculated value of unit cell volume was found to be 834.4867 Å^3, which is very close to the standard value (834.57 Å^3). The calculated average micro-strain and dislocation density was 6.01×10^{-3} and 2.33×10^{-3}, respectively, which deduced the crystallographic defect imperfection in the crystal structure.[38]

The Raman spectra of the prepared Mn_2O_3 is given in Fig. 4. The presence of five well resolved peaks are located at 343, 530, 569, 633 and 749 cm^{-1}, which are characteristic spectral features of Mn-based oxide. Raman shifts at 343 and 633 cm^{-1} can be qualified as asymmetric stretching of bridge oxygen species (Mn–O–Mn) and symmetric stretching of Mn_2O_3 groups, respectively.[39] The peak located at 569 cm^{-1} represented the terminal Mn–O stretching in the basal plane of MnO_6 sheet in the MnO_2 skeleton.[40] Other peaks were observed due to the mixture of a small amount of Mn_3O_4 in the prepared Mn_2O_3,[41] which complemented the results of previously discussed XRD. Therefore, the prepared Mn_2O_3 is a mixture of Mn_2O_3, MnO_2 and Mn_3O_4.

To understand the surface chemical composition of prepared Mn_2O_3, XPS was carried out. Fig. 5(a) shows the total XPS survey scan of prepared Mn_2O_3 within a binding energy range of +1350 to −10 eV. The presence of Mn (945.03, 902.86, 849.22, 772.32, 652.63, 641.47, 82.09, and 47.05 eV) and O (1011.39, 995.27, 975.11, and 531.69) was confirmed with a negligible amount of C (1223.17 and 284.26 eV) and Cl (1301.93, 267.51, and 198.68 eV). The amount of Mn and O was 34.11% and 51.26%, respectively (by the no. of atoms present). The ratio of Mn and O is very close to Mn_2O_3. C might come from calcination of the adhered shell of the reverse micelle during filtration of $MnCO_3$ and the presence of Cl might be derived from tap water contamination during the course of apparatus cleaning.

From Fig. 5(b), two sharp and well defined peaks at 652.81 and 641.63 eV indicated Mn $2p_{1/2}$ and Mn $2p_{3/2}$ states having a separation of 11.15 eV. A small broad satellite peak at

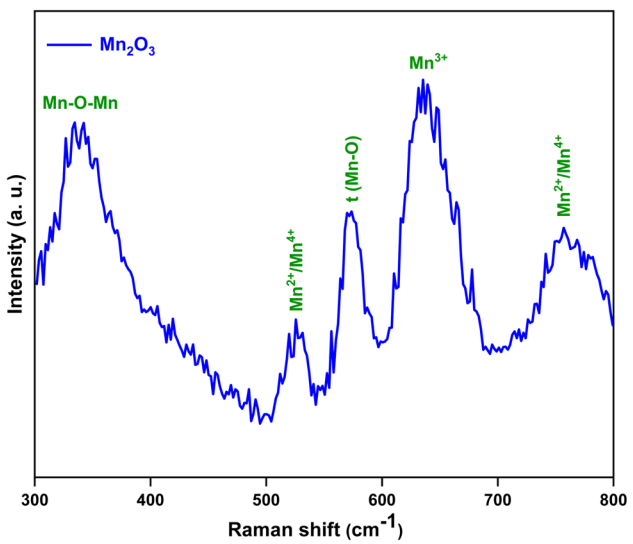

Fig. 4 Raman spectrum of the prepared Mn_2O_3.

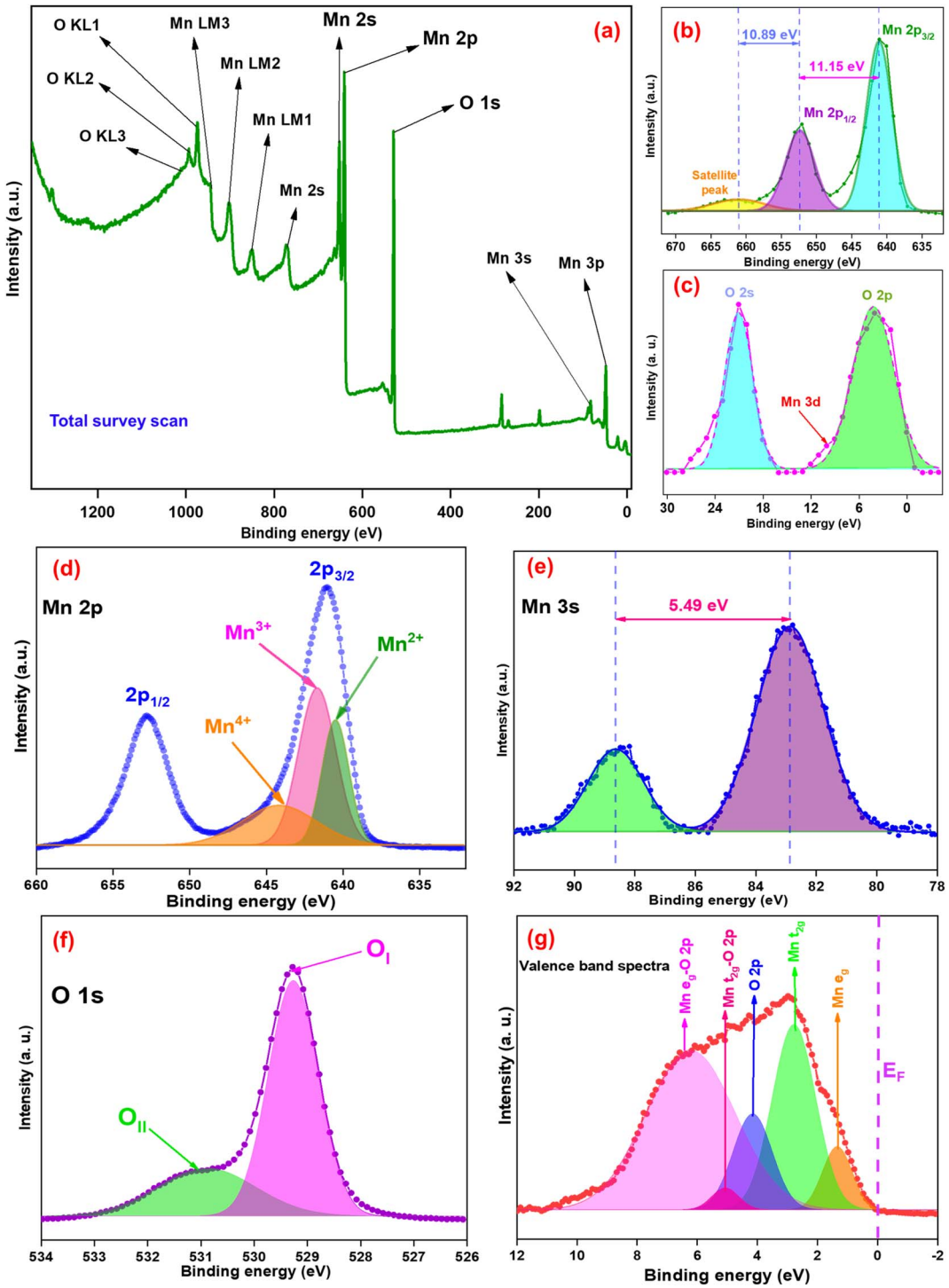

Fig. 5 XPS survey for prepared Mn_2O_3. (a) Complete scan, (b) Mn region and (c) valence band region. Core level XPS narrow spectra for (d) Mn 2p, (e) Mn 3s, (f) O 1s states and (g) valence band region. Original spectra (lines with tiny circles) and Gaussian deconvolution (fitted with the covered area).

661.14 eV that is 10.89 eV higher than that of Mn 2p state confirmed the presence of the Mn^{3+} oxidation state. Therefore, the prepared Mn_2O_3 could be Mn_2O_3 with a mixture of Mn(II), Mn(III) and Mn(IV) oxidation states. At the lower energy level [Fig. 5(c)], two sharp and well defined peaks at 21.05 and 4.18 eV were for the O 2 s and O 2p state with the Mn 3d state indicated by a tailing peak at 9.91 eV. These values are well matched with previously reported values.[42,43]

To understand the oxidation states of Mn, core level binding energy narrow spectra were taken [Fig. 5(d)–(f)]. All the Mn 2p, Mn 3s and O 1s spectra were broad due to multiple splitting. The presence of Mn^{4+}, Mn^{3+}, and Mn^{2+} was confirmed by Gaussian fitted peaks at 643.78, 641.63 and 640.54 eV,

respectively. The values of multiple splitting energies of the Mn 3s spectra were 88.47 and 82.98 eV, with a distance of 5.49 eV. This peak splitting arose by the coupling of non-ionized 3s electron with 3d valence-band electrons. This splitting is directly proportional to the remaining electron in the 3s orbital and other unpaired electrons having parallel spins. The energy

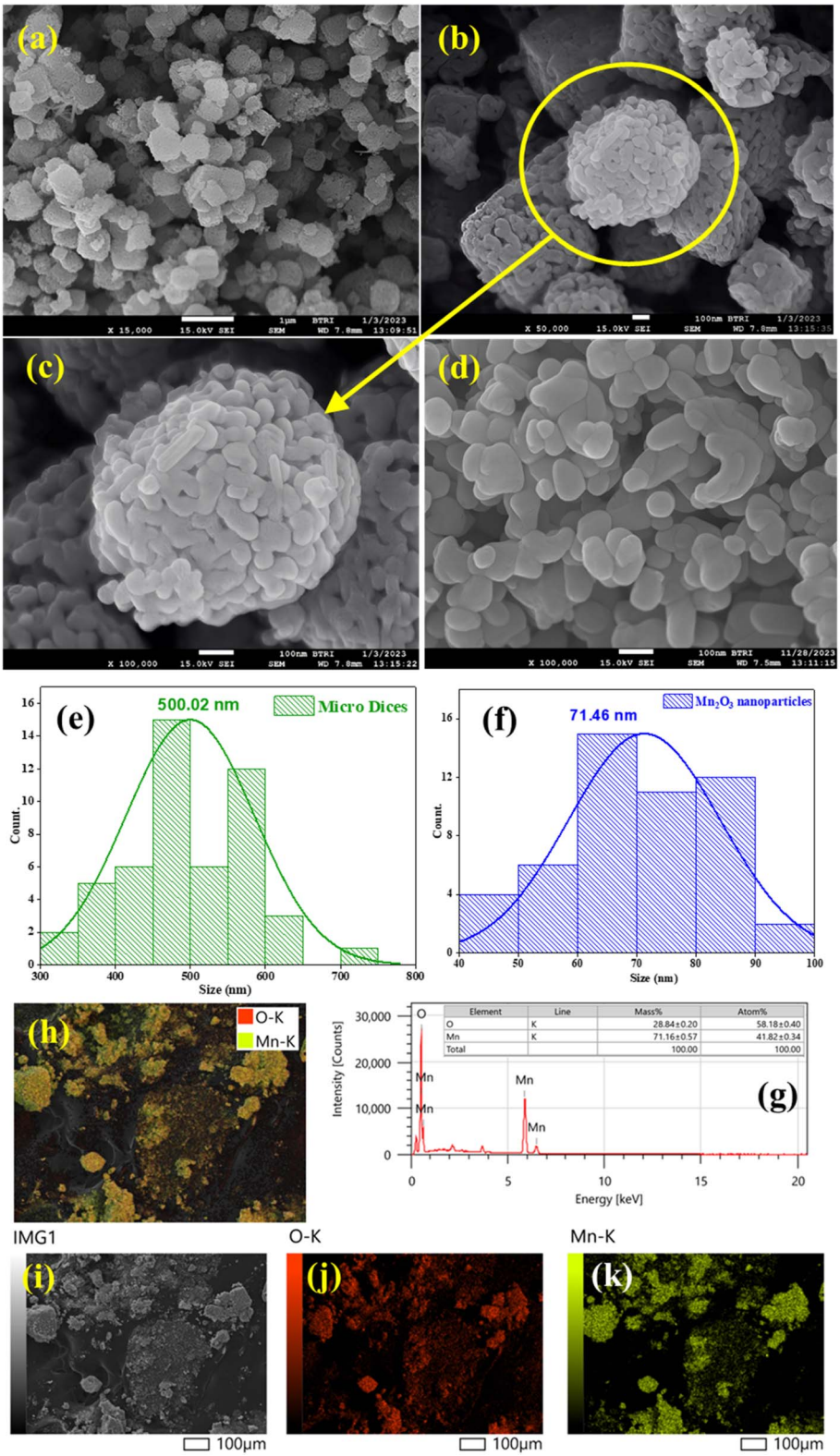

Fig. 6 FESEM image (before grinding) at a scale bar of (a) 1 µm and (b and c) 100 nm and after grinding at a scale bar of (d) 100 nm. Histogram before (e) and after (f) grinding. (g) EDX spectrum showing the % of major elements. Elemental mapping of the prepared Mn_2O_3 through (h) whole mapping, (i) selected area, and coverage of (j) O and (k) Mn.

Table 3 Comparison of experimental and theoretical values with respect to the fraction of Mn and O present in the prepared Mn_2O_3

Fraction of atoms	Theoretical values				Experimental values	
	Mn_2O_3	Mn_5O_8	MnO_2	Mn_3O_4	XPS	EDX
Mn/O	**0.6666**	0.6250	0.5000	0.7500	**0.6654**	0.7188

difference of this splitting designated the particular state of Mn. In this case, the formation of the Mn_2O_3 phase was confirmed due to the Mn^{3+} oxidation state. Narrow peaks appearing at binding energies of 530.83 eV (O_{II}) and 529.26 eV (O_I) in O correspond to the Mn–O–Mn bond of manganese oxide. The broad peak of O_{II} at lower intensity corresponds to Mn–OH bonding. The presence of the –OH group in the O 1s narrow spectra was due to the absorption of moisture of prepared Mn_2O_3. Fig. 5(g) shows the valence band spectra of prepared Mn_2O_3. The valence band maximum (VBM) positions were determined by Gaussian deconvolution of the leading peak edges. Here, the binding energy of Mn e_g of the Mn 3d orbital is 1.32 eV higher than the Fermi level (E_F). Some other states were also found: Mn t_{2g}, O 2p, Mn t_{2g}-O 2p, and Mn e_g-O 2p were at binding energies of 2.75, 4.16, 5.05, and 6.33 eV. This result indicated the primary formation of Mn_2O_3, with a small amount of MnO_2 and Mn_3O_4 mixed with it, which also complemented the results of % of Mn and O already acquired from XPS spectral data.[43,44]

The surface morphology and average particle size were assessed using FESEM. Fig. 6(a–d) shows the surface morphology of Mn_2O_3 before and after grinding. Before grinding, the particles were distorted porous microdice with a histogram average size of 500.02 nm [Fig. 6(e)]. Tiny Mn_2O_3 nanoparticles aggregated with each other, resulting in porous Mn_2O_3 microdice. After breaking the microdice, the histogram showed Mn_2O_3 particles of an average size of 71.46 nm [Fig. 6(f)]. In this case, all the particles were of different shapes and sizes.[45,46] In the reverse micelle core, only water exists. The water media of the reverse micelle core might generate $MnCO_3$. Calcination of $MnCO_3$ at 400 °C produced Mn_2O_3, releasing CO_2. As predicted, CO_2 emission did not affect the reactor core's structure, leaving a porous micro dice of 500.02 nm. Ultrasonic waves twisted the reactor core from a spherical shape to a somewhat distorted cube-like dice shape. Some fractured dice were also observed in Fig. 6(b), which arose during transfer of the sample after calcination.

The composition and stoichiometry of prepared Mn_2O_3 were examined with the help of the energy dispersive X-ray microanalysis (EDX) technique. Fig. 6(g) portrays the EDX spectrum of prepared Mn_2O_3. The presence of Mn and O were established as major elements with a very small amount of impurities. These elements were uniformly distributed over the whole Mn_2O_3 sample, as confirmed by the elemental mapping illustration in Fig. 6(h–k). The EDX lines located at 5.9 and 0.53 keV are the K lines of Mn and O, respectively. The quantification result from EDX data revealed the percentage of each element with corresponding energy distribution held in the matrix enabling us to determine the composition of the prepared sample. Here, Mn and O are the main components and the % of atoms for Mn and O are 41.82 and 58.18%, respectively, which is almost 2 : 3, and suggests that the prepared Mn_2O_3 could be primarily Mn_2O_3 with a small amount of other manganese oxides (Mn_5O_8, MnO_2 and/or Mn_3O_4) within it.[47,48] The literature says that Mn_2O_3 belongs to the orthorhombic system with MnO as the basic unit, where Mn^{3+} exhibits an octahedral coordination and O^{2-} shows a tetrahedral coordination. Mn_2O_3 also suffers a phase transition from an orthorhombic structure to a layered structure of MnO_2. Therefore, Mn_2O_3 could be considered as an individual constituent and/or as a combination of MnO and MnO_2. Similarly, Mn_3O_4 possesses two oxidation states, Mn^{2+} and Mn^{3+}, that could be individual constituents and/or a combination of MnO and Mn_2O_3.[49] The elemental composition of prepared Mn_2O_3 were compared with the theoretical values. Because XPS provides more convenient and detailed results as compared to EDX, the results from Table 3 confirmed that the prepared product is mainly Mn_2O_3.

TEM was performed to rationalize the FESEM and XRD results. Fig. 7 shows the TEM graphs of the prepared Mn_2O_3 nanoparticles. The particles are dice shaped with different sizes. Two dice were clearly seen and drawn in [Fig. 7(a)]. These dice are composed of small discrete particles, which supports the FESEM result. Distinguishable crystal planes are observed in Fig. 7(b, e and j), indicating good crystallinity of the Mn_2O_3 nanoparticles. Five cross-sections of these three micrographs were analyzed using ImageJ software. The FFT images (Fig. 7c, f, h, k and m) and line intensity plots (Fig. 7 d, g, i, l, n and o) of the corresponding cross-sections revealed six planes [(020), (040), (132), (022), (343), and (222)], of respective *d*-spacing (0.47, 0.23, 0.25, 0.34, 0.16, and 0.27 nm). These values are well matched with COD-pdf# 96-210-5792.[50]

The solid-state UV-visible spectra for the prepared Mn_2O_3 nanoparticles has an absorption maxima at 351.84 nm, as shown in Fig. 8(a). From the optical absorption maxima (A), the absorption coefficient (α) was calculated using eqn (7):

$$\alpha = \frac{A}{d} \tag{7}$$

where d = thickness of the sample. According to Tauc's eqn (8) (ref. 51 and 52) for allowed direct transitions, the photon dependency of the absorption coefficient could be obtained:

$$(\alpha h\nu)^2 = B(h\nu - E_g) \tag{8}$$

where B = is the transition probability, and E_g = optical energy gap. Fig. 8(b) portrays the relationship absorption coefficient $(\alpha h\nu)^2$ *vs.* $h\nu$ of the prepared Mn_2O_3 nanoparticles. The intercept of the inclined straight line with the photon energy axis delivered the value of the optical band gap, which was 3.21 eV. This is considered to be a low band gap within the range of semiconducting material, which makes them suitable for electrochemical energy storage applications.[53]

To determine the nature of the electrochemical reaction in the cell, CV was performed within the potential window +1.0 V to +2.2 V at scan rates of 0.6, 0.7, 0.8, 0.9, and 1.0 mV s^{-1}

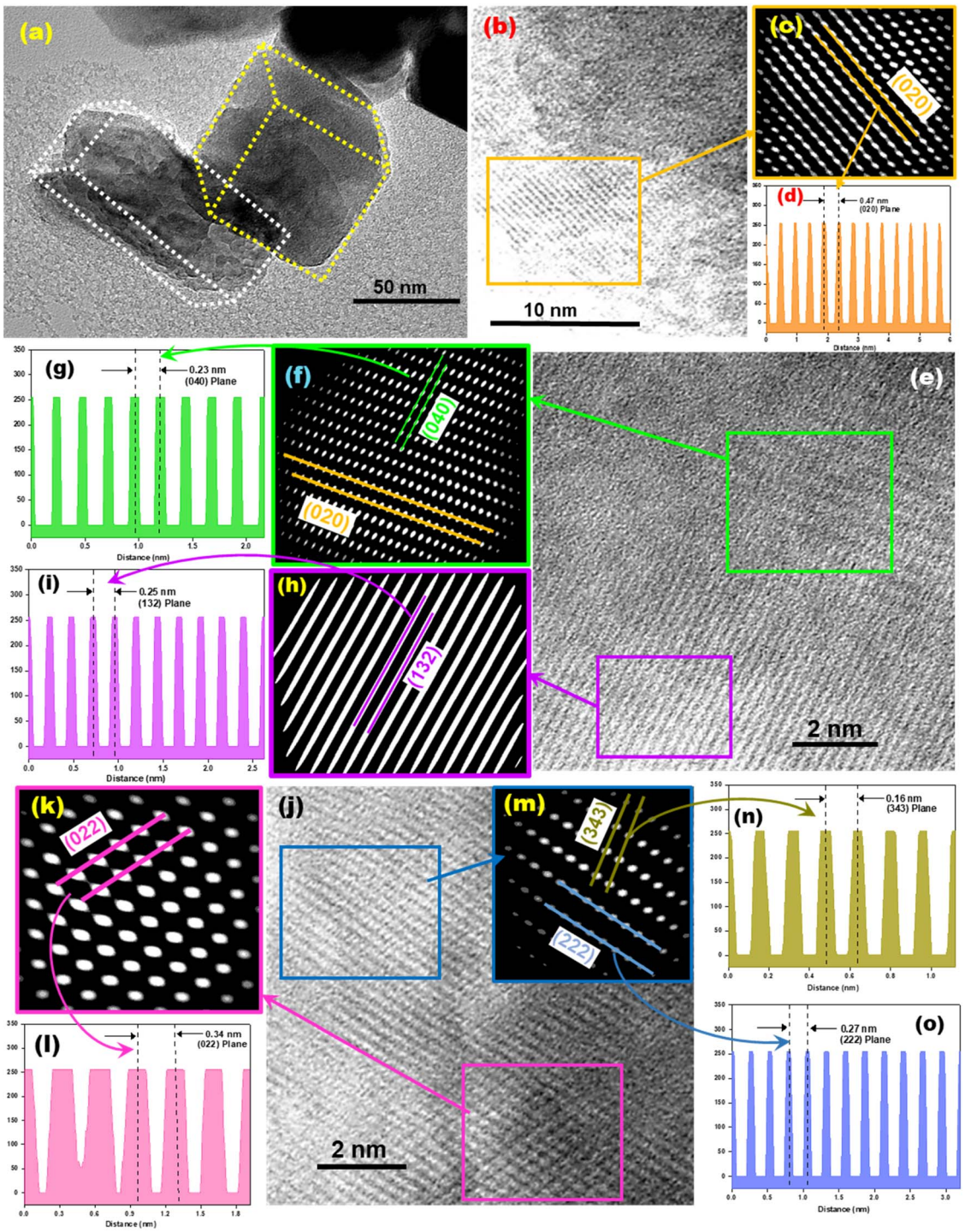

Fig. 7 TEM image of the prepared Mn_2O_3 at different magnifications: scale bars of (a) 50 nm, (b) 10 nm, and (e and j) 2 nm. (c, f, h, k and m) FFT images of corresponding cross sections (b, e and j). (d, g, i, l, n and o) Line intensity plots of corresponding crystal planes from FFT images indicated by different colors.

(Fig. 9(a)). A pair of well resolved redox peaks were noticed. The heights of the anodic and cathodic peaks were close to each other at every scan rate, which implied the strong reversibility of the cell reaction. At all scan rates, similar anodic peak and cathodic peaks were observed in the range of +1.68 to +1.75 V and +1.21 to +1.16 V, respectively. The reactions[54] of the anodic and cathodic peaks could be assigned as follows:

Anodic reaction:

$$x\mathrm{Zn} \leftrightarrow x\mathrm{Zn}^{2+} + 2x\mathrm{e}^{-}$$

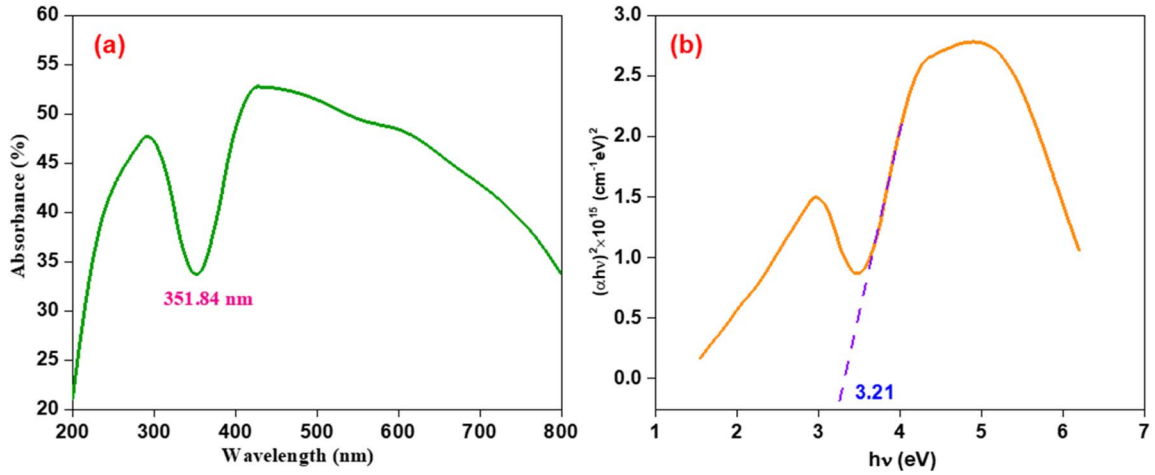

Fig. 8 (a) Absorption spectra, and (b) absorption coefficient $(\alpha h\nu)^2$ *vs.* hν for the prepared Mn_2O_3 nanoparticles.

Cathodic reaction:

$$H_2O \leftrightarrow H^+ + OH^-$$

$$Mn_2O_3 + xZn^{2+} + 2xe^- \rightarrow Zn_xMn_2O_3$$

$$4Zn^{2+} + 6OH^- + SO_4^{2+} + 5H_2O \leftrightarrow Zn_4(OH)_6(SO_4)\cdot 5H_2O$$

The peak heights increased with faster scan rates, and the anodic peaks shifted towards the right while cathode peaks shifted to the left, demonstrating the possible slight adsorption

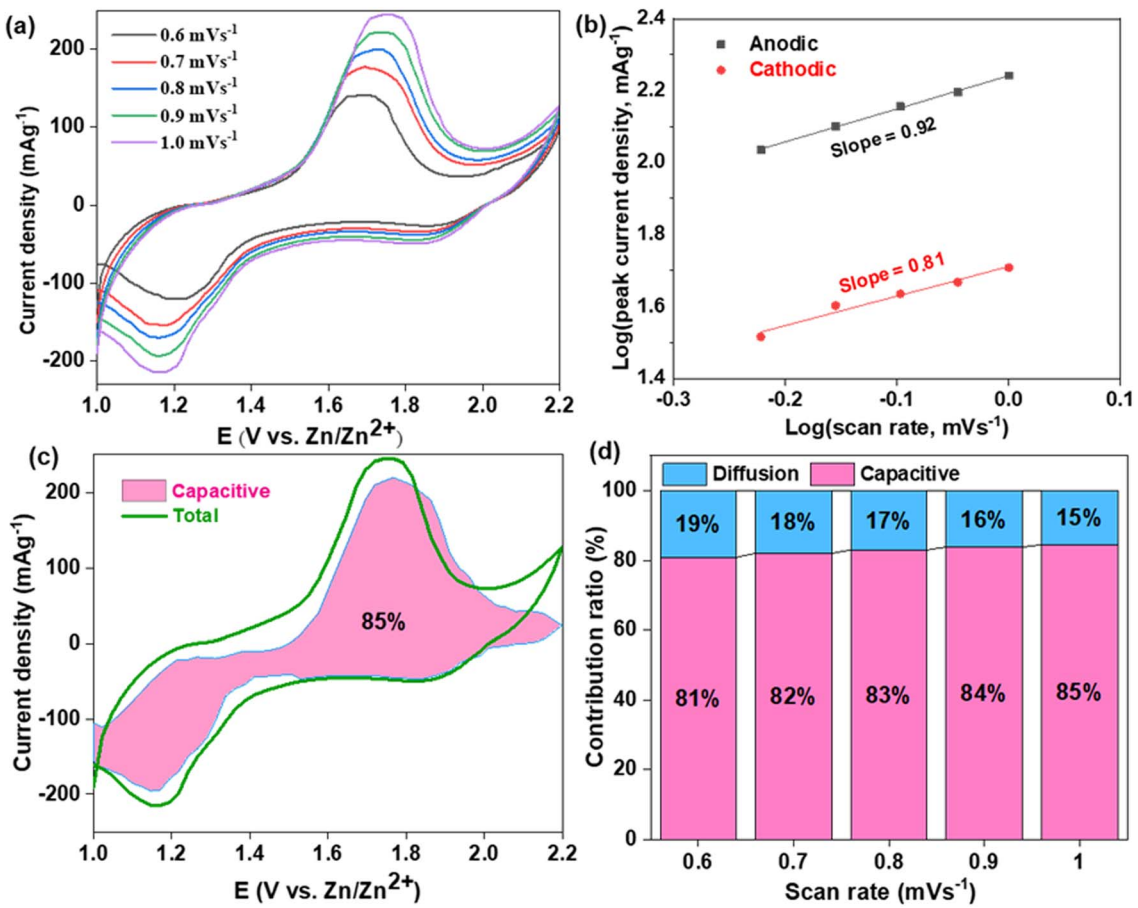

Fig. 9 CV of the fabricated CR-2032 coin cell (a) at different scan rates. (b) Log(peak current density) *vs.* log(scan rate) with a fitted line. (c) Capacitive contribution with respect to total capacity. (d) Percentages of capacitive and diffusion contribution at different scan rates.

of Zn^{2+} ions onto the cathode surface responsible for Zn^{2+} ion storage. Dunn's method was used to test the CV using eqn (9):

$$\text{Log } i = \log a + b \log \nu \quad (9)$$

where i = peak current density, ν = scan rate, and a and b = constants. The value of b lies within 0.5 to 1.0. The closer the value of b to 0.5, the more the diffusion-controlled behavior (Q_d), while the closer the value of b to 1.0, the more it resembles capacitive behavior (Q_c). From the CVs, a log ν *vs.* log i graph was plotted [Fig. 9(b)], and the value of the slope, $b = 0.92$ and 0.81 for anodic peaks and cathodic peaks, respectively, are much closer to 1.0 rather than 0.5. This indicated that the electrochemical Zn^{2+} storage mechanism included diffusion controlled pseudo capacitive behavior.[55,56] Mn_2O_3 nanoparticles provided a superior non-diffusion storage mechanism limited to Zn^{2+} ions. The percentages of the capacitive and diffusion contribution ratios can be determined using eqn (11):

$$i_p(\nu) = k_1\nu + k_2\nu^{\frac{1}{2}} \quad (10)$$

or

$$\frac{i_p}{\nu^{\frac{1}{2}}} = k_1\nu^{\frac{1}{2}} + k_2 \quad (11)$$

where k_1 = slope and k_2 = intercept of $\nu^{\frac{1}{2}}$ *vs.* $\frac{i_p}{\nu^{\frac{1}{2}}}$ plot. The diffusion contribution or pseudo-charge storage is $k_1\nu$, and the capacitive contribution or insertion type capacity is $k_2\nu^{\frac{1}{2}}$.[57,58] The CV for capacitive contribution was approximately 85% that of the total contribution at a scan rate of 1.0 mV s^{-1} [Fig. 9(c)]. The capacitive contribution rates were increased with the scan rates. At 0.6, 0.7, 0.8 0.9, and 1.0 mV s^{-1}, the capacitive contributions were 81, 82, 83, 84, and 85%, respectively [Fig. 9(d)], which represented the (de)intercalation dominated cell reaction.[59]

The CV experiment was performed at the electrochemical window of +1.0 to +2.2 V and a pair of redox peaks were seen within the electrochemical window of +1.0 to +1.8 V. Therefore, the BCD experiment was performed in the electrochemical window of +1.0 to +1.8 V and this window was fixed for all BCD experiments. Here, the potential window and applied current

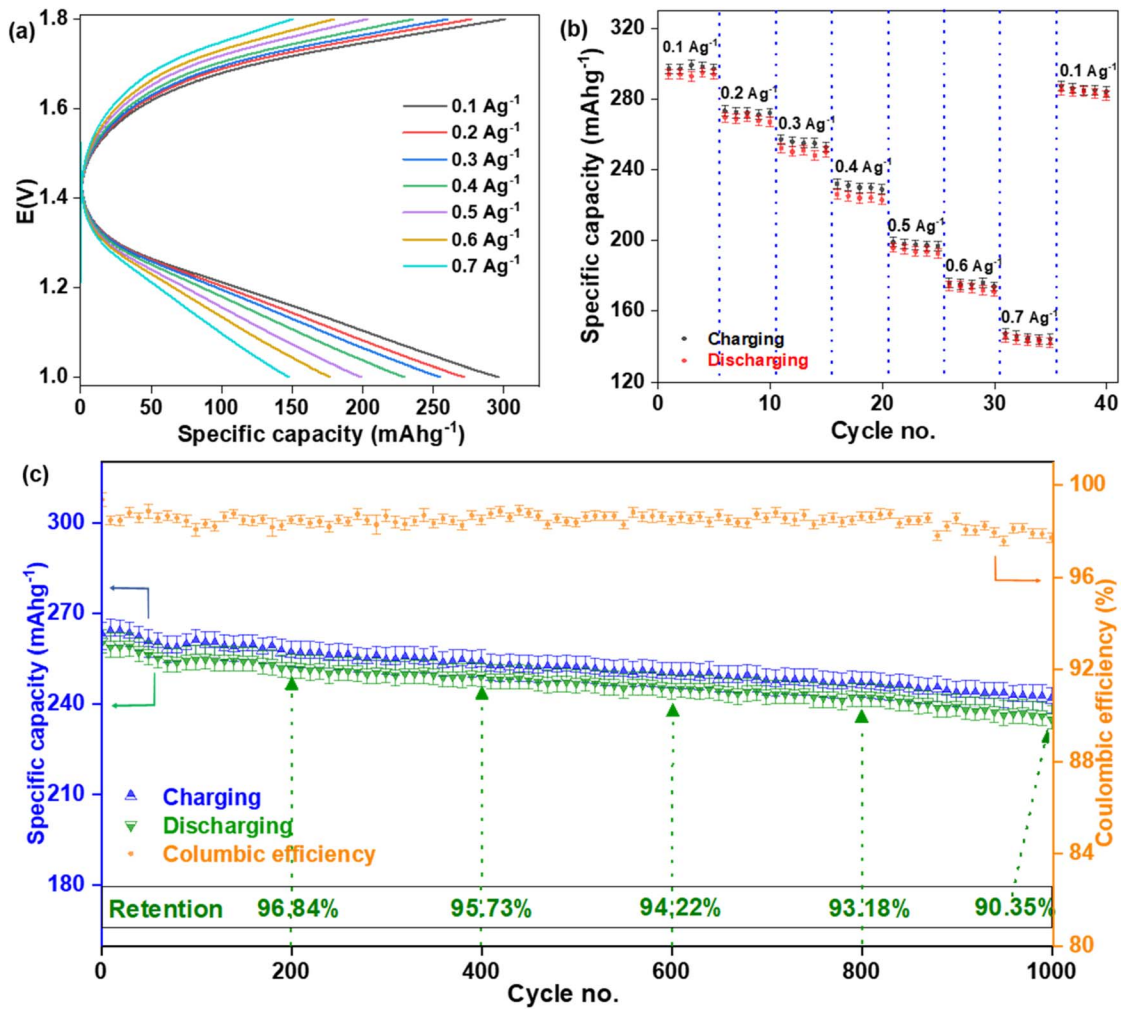

Fig. 10 BCD of the fabricated CR-3032 coin cell. (a) Specific capacities and (b) rate capability at different current densities. (c) Cycling performance at 0.3 A g^{-1} for 1000 cycles.

density were fixed, while time was a variable and the specific capacities were different depending on how much time was needed for every cycle. This type of BCD is very similar to the chrono-potentiometric experiment. BCD curves of the fabricated CR-2032 coin cell tested at various current density are displayed in Fig. 10(a). The specific discharge capacities decreased (293.59 ± 4.75, 269.47 ± 4.62, 252.10 ± 4.66, 225.82 ± 4.91, 195.69 ± 4.38, 173.98 ± 4.49, and 144.83 ± 4.47 mA h g^{-1}) as the applied current density increased (0.1, 0.2, 0.3, 0.4, 0.5, 0.6, and 0.7 A g^{-1}), respectively. The rate capability was also performed at those current densities [Fig. 10(b)]. When the applied current density dropped back from 0.7 to 1.0 A g^{-1}, the cell delivered a specific discharge capacity of 284.96 ± 4.91 mA h g^{-1}, which retained 96.76% of its initial value of 293.59 ± 4.75 mA h g^{-1}. This experiment was done on three different coin cells and the statistical values are represented in Table S1.† Cycling was done at 0.3 A g^{-1} current density for 1000 cycles on three different coin cells and the results are represented in Table S2.† The coulombic efficiency was maintained at an average of 98.44 ± 0.37%. After 200, 400, 600, 800, and 1000 cycles, the specific discharge capacity retention was calculated to be 96.84%, 95.73%, 94.22%, 93.18% and 90.35%, respectively.[60,61] The discharge capacity is slightly lower than the charging capacity for every cycle. It could be concluded that a small amount of Zn^{2+} ion might have been trapped in the Mn_2O_3 cathode and/or formed stable complexes with it after every charging–discharging process, which blocked the available (de)intercalation sites.

EIS was performed to find out the conductivity/resistance of the fabricated coin cell at a potential of +1.9 V at a frequency region between 300 kHz to 100 mHz. The Nyquist plot [Fig. 11(a)] was tested by using equivalent circuit $R_1 + Q_2/R_2 + Q_3/R_3 + W_4$. Here, R_1 = solution resistance (R_s) in ohms, R_2 = electrode resistance (R_f) due to solution electrolyte interface contribution in ohms, R_3 = charge transfer resistance (R_{ct}) in ohms, Q_2 and Q_3 = capacitance of the cathode in F considered as porous material, which is conventionally represented as constant phase elements (CPE), and W_4 = Warburg impedance (W_s) in ohm $s^{1/2}$. The values of R_s, R_f, R_{ct}, and W_s were found to be 7.05, 50.74, 9.021 Ω, and 28.301 Ω $s^{1/2}$, respectively for fresh coin cells, and those of BCD after 1000 cycles were 7.812, 67.04, 63.77 Ω, and 15.65 Ω $s^{1/2}$, respectively. Fresh cells showed lower resistances compared with the used cells. The equivalent circuit almost fitted to the Nyquist plot at higher frequency but deviation was found at lower frequency. This discrepancy could be the reason for the possible development of secondary capacitors within the cell. Certain cathode materials might have separated from their current collector during the consecutive charging-discharging phase, combined with the electrolyte, passed through the separator, and moved towards the anode surface. As the resistances were comparatively higher after 1000 cycles, some detached cathode material might form a stable layer on the surface of the anode, which might be the reason for decreasing the capacity retention as the cycling continued. In addition, the mass transport system could be non-uniform within the cell. To test the validation of impedance fitting parameters, the Kramers–Kronig equation was used by checking error analysis. The plot of Z_{real} *vs.* frequency of impedance [Fig. 11(b)] completely satisfied the validation. The plot of Z_{im} *vs.* frequency of impedance [Fig. 11(c)] also satisfied the validation but showed a small deviation at higher frequency. These results showed the reliability of the measurement since it satisfied the linearity, causality and stability for impedance measurements.[62,63]

The relationship of Z_{real} and the reciprocal square root of the angular frequencies ($\omega^{-1/2}$) is expressed in eqn (12):

$$Z_{re} = R_f + R_{ct} + \sigma_\omega \omega^{-\frac{1}{2}} \quad (12)$$

where, σ_ω = the Warburg impedance coefficient. The plot of $\omega^{-\frac{1}{2}}$ *vs.* Z_{re} was constructed before and after BCD cycling [Fig. 11(d)]. This portrays the resistance in the lower frequency region of the coin cell based on the movement of Zn^{2+} ions within the cell. The value of the slopes (σ_ω) were 11.74 and 15.50 Ω $s^{1/2}$ before and after BCD cycling, respectively.

The diffusion coefficient of Zn^{2+} ions into the bulk electrolyte was calculated using eqn (13):

$$D = 0.5(RT/AF\sigma_\omega C)^2 \quad (13)$$

The double layer capacitance was calculated using eqn (14):

$$Z_{re} = R_s + R_{ct} + 2\sigma_\omega{}^2 C_{dl} \quad (14)$$

$$\omega = \frac{1}{R_{ct} \cdot C_{dl}} \quad (15)$$

where R = gas constant, F = Faraday's constant, T = absolute temperature, D = diffusion coefficient, C = molar conc. of Zn^{2+} ions, C_{dl} = double layer capacitance, and A = area of cathode surface. The values of C_{dl} were found to be 41.7×10^{-6} and 6.713×10^{-3} F before and after BCD cycling of 1000 cycles, respectively. Moreover, the exchanged current density was calculated by eqn (16):

$$i^0 = \frac{RT}{nF} R_{ct} \quad (16)$$

where n = no. of electrons involved in the (de)intercalation process. The calculated values of the exchanged current density was found to be 1.12×10^{-1} and 8.19×10^{-1} A before and after BCD, respectively.[64,65]

The Bode plot of frequency dependent impedances [Fig. 11(e)] showed that it remained at a lower resistance at higher frequency with inclined lines at lower frequency, which indicated a good capacitive of Zn^{2+} ion storage of the prepared Mn_2O_3 nanoparticles. The Bode plot of frequency dependent phase angles [Fig. 11(f)] showed that the highest phase angles were 31.02° and 37.53° before and after BCD, respectively, which represented the pseudocapacitive behavior of semiconducting Mn_2O_3 nanoparticles for Zn^{2+} ion storage within the cell.[66]

To understand the reaction mechanism inside the coin cell, post-mortem characterization of the cathode material was done. After BCD was done, the coin cell was broken using a sharp needle and hammer. The cathode material was taken, washed with DI water, and sent for further analysis. First, SEM

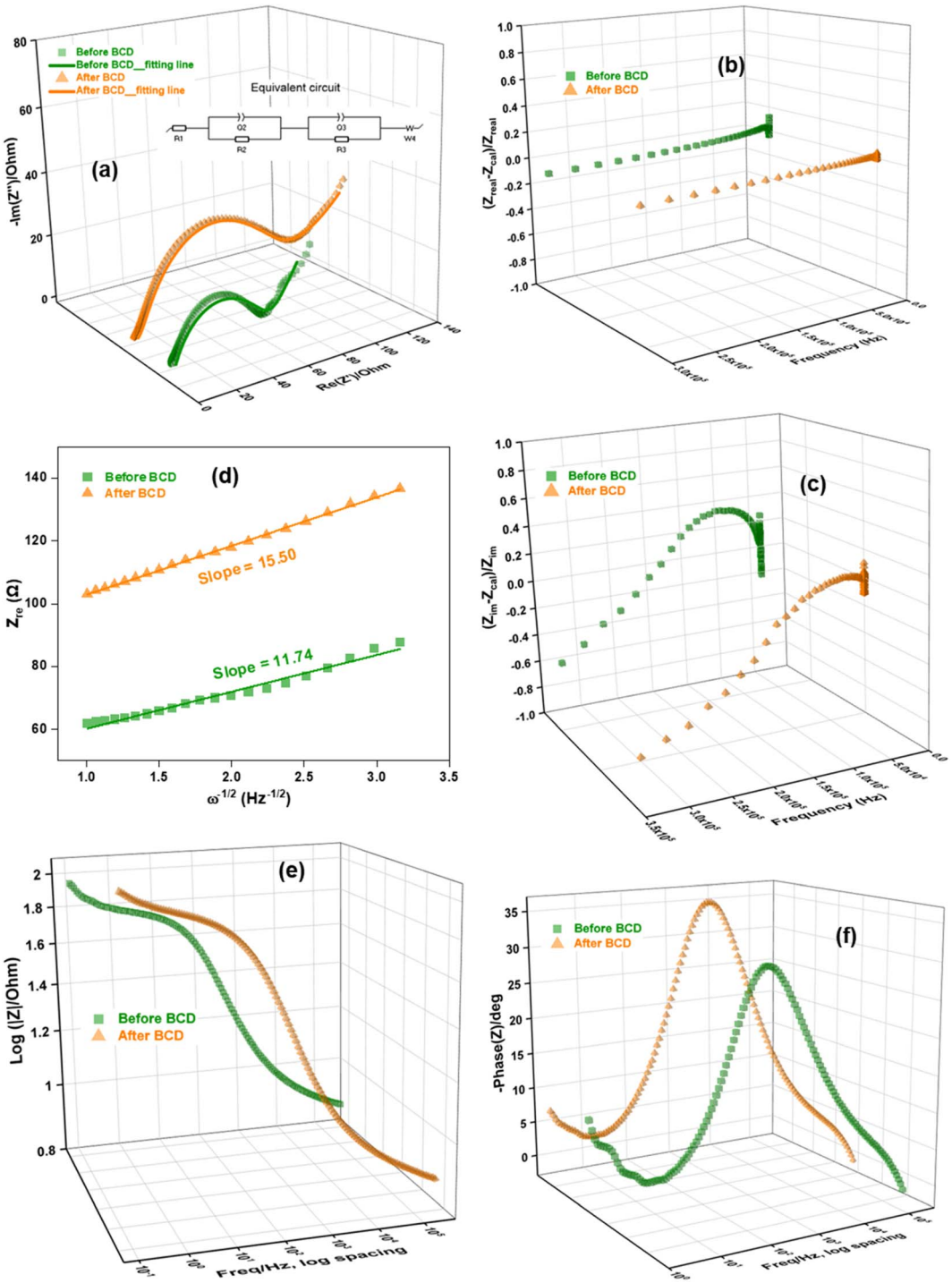

Fig. 11 EIS of the CR-2032 coin cell. (a) Nyquist plot with an equivalent circuit. Error analysis for (b) Z_{real} and (c) Z_{im} *vs.* frequency of impedances. (d) Plot of Z_{real} *vs.* reciprocal square root of angular frequency ($\omega^{-1/2}$). Bode plots of frequency dependent (e) impedances and (f) phase angles.

images and EDX profiles of the cathodes were analyzed before (fresh cathode) and after BCD (used cathode). Fig. 12(a–d) shows SEM images of fresh and used cathodes. For the fresh cathode, particles of different sizes and shapes were present and the distribution of particles were almost homogeneous (Fig. 12(a and c)). After BCD, the cathode showed non-homogeneous distribution of particles (Fig. 12(b)), the surface of the cathode was covered by powder like substances or some foreign substances were trapped inside the cathode (Fig. 12(d)). This result implied that the cathode underwent some internal or surface changes while charging-discharging. For better understanding, EDX measurements were taken. The cathode before and after BCD showed almost similar percentages of Mn and O, with small amounts of C and F because bixbyite was

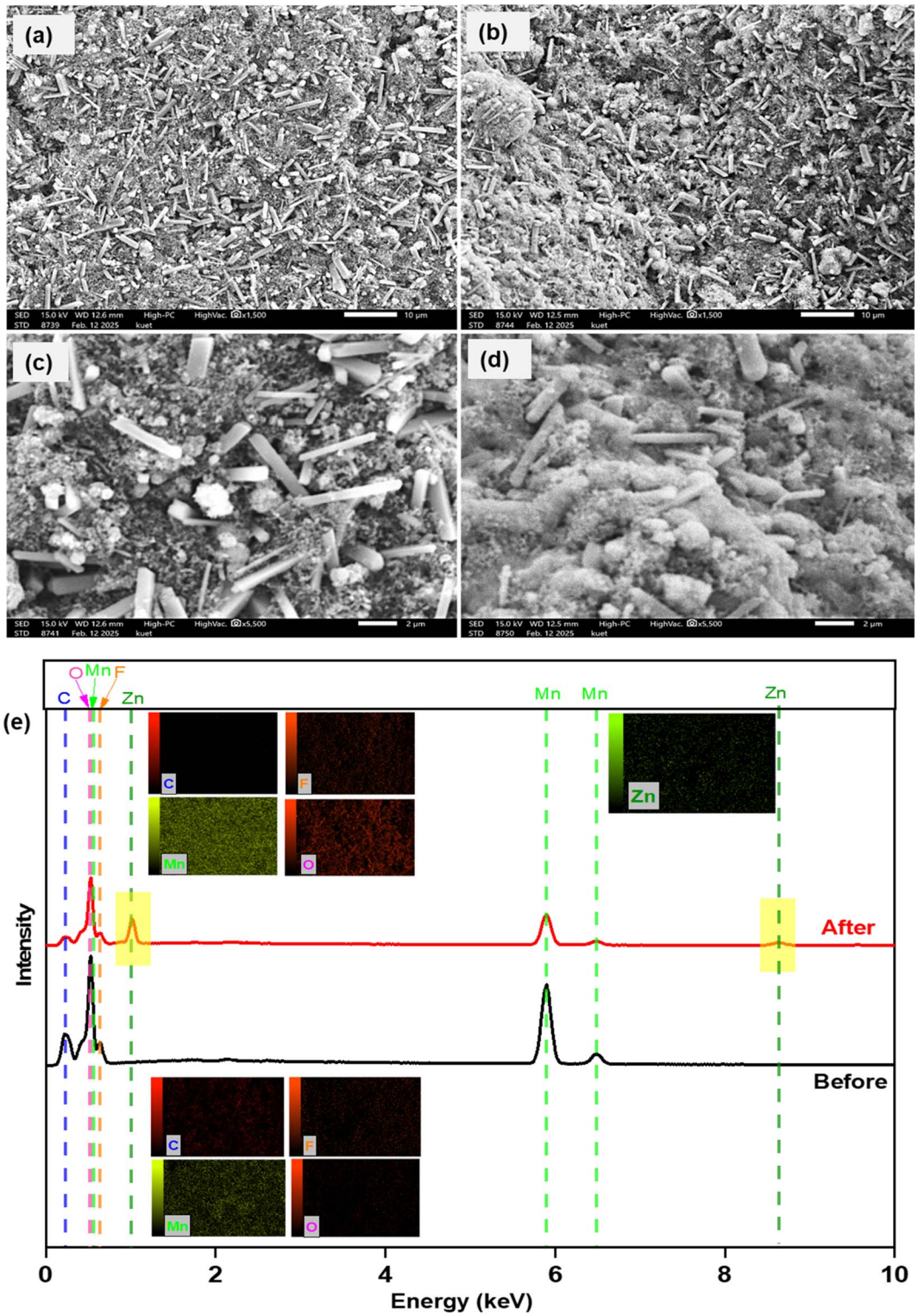

Fig. 12 SEM images of the cathode before ($a = 10$ μm, $c = 2$ μm) and after ($b = 10$ μm, $d = 2$ μm) BCD. (e) Corresponding EDX data: inset showing elemental mapping.

mixed with PVDF and NMP, resulting in the presence of C and F with Mn and O. Zn was present in the used cathode (after BCD) while it was absent in the fresh cathode (before BCD). This might be explained in terms of the decrease of retention from 100% after BCD. There could be some intermediate product formation with the (de)intercalation of Zn^{2+} ions in the bixbyite framework. The reaction within the cell was not completely reversible and responsible for the presence of Zn in the form of

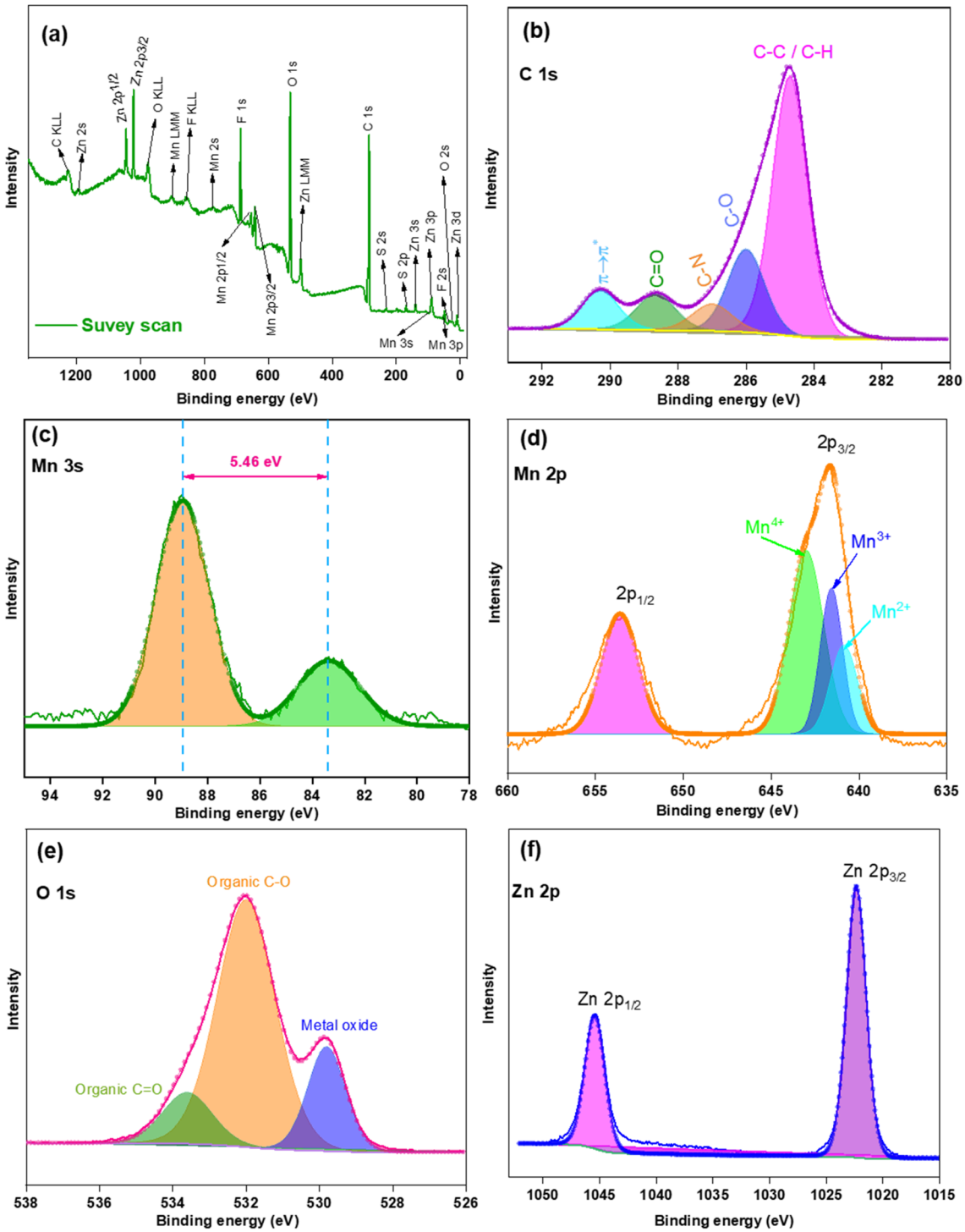

Fig. 13 XPS survey for the cathode material after BCD (a) survey scan. Narrow spectra of (b) C 1s, (c) Mn 3s, (d) Mn 2p, (e) O 1s and (f) Zn 2p. Original spectra (lines with tiny circles) and Gaussian deconvolution (fitted with covered area).

$Zn_xMn_2O_3$ within the cathode and decreased BCD cycling retention after 1000 cycles.

A part of the used cathode was sent for XPS analysis (Fig. 13). Survey scans [Fig. 13(a)] indicated the presence of Mn, O, C, Zn, F, N, and S at 3.61, 26.88, 56.28, 2.93, 8.77, 0.62, and 0.86%, respectively (by no. of atoms present). The huge amount of C was present for C-black. Fig. 13(b) indicated a narrow spectra of C 1s with Gaussian deconvolution fitting curves. The presence of sp^3 C for C–C or C–H was at 284.71 eV while C–O, C–N, and C=O were found at 285.99, 287.01, and 288.66 eV, respectively.[67] These groups arose from PVDF and NMP. A shake up satellite peak at 290.27 eV indicated the presence of $\pi \rightarrow \pi^*$

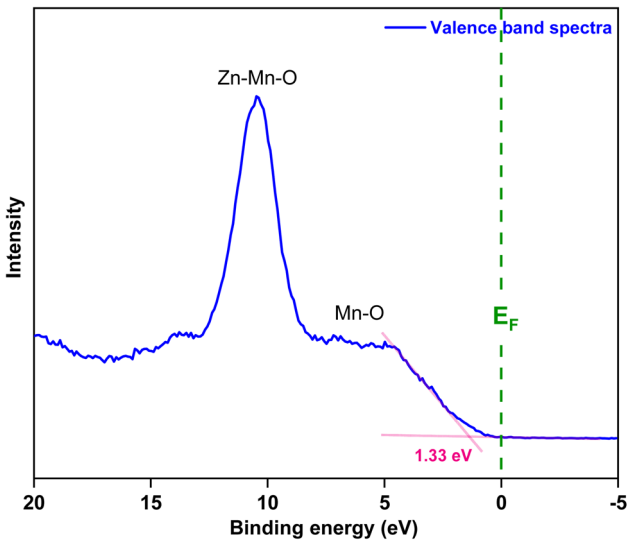

Fig. 14 XPS valence band spectra of the cathode material after BCD.

and explained the aromatic character of C in NMP. Therefore, the presence of C, N, O, and F was because of the additives used for coin cell fabrication. Fig. 13(c) showed that the Mn 3 s spectra exhibited two sharp well defined peaks (88.91 and 83.45 eV) with a separation of 5.46 eV, which that Mn_2O_3 was in a Mn^{3+} oxidation state. Fig. 13(d) showed two well defined peaks at 653.55 and 641.65 eV for Mn $2p_{1/2}$ and Mn $2p_{3/2}$. The separation of 11.9 eV is slightly higher than the results obtained from the raw bixbyite micro dice [Fig. 5(d)]. Gaussian deconvolution fitting peak of Mn $2p_{3/2}$ showed the presence of Mn^{4+}, Mn^{3+}, and Mn^{2+}, which is similar to the previous deconvolution peak for raw bixbyite micro dice, but the peak area of Mn^{4+} seems to be greater than Mn^{2+}, which differs from raw bixbyite micro dice where the peak area of Mn^{2+} seems to be greater than Mn^{4+}. Therefore, it could be said that there might be an internal chemical change during charging-discharging. Fig. 13(e) showed the presence of peaks at 533.64 and 532.01 eV for organic C=O and C–O, responsible for NMP, and the peak at 529.81 eV indicated the presence of Mn-oxide. From Fig. 13(f), two sharp peaks at 1045.38 and 1022.32 eV indicated that Zn $2p_{1/2}$ and Zn $2p_{3/2}$ states exhibited a separation of 23.06 eV.[68] Here a small percentage of Zn is present with a tiny percentage of S, is a foreign material that was not used during cathode preparation. During the coin cell fabrication, $ZnSO_4$ was used as electrolyte but the cathode was washed with DI water after the used coin cell was broken. Therefore, the remaining Zn and S was expected to be washed off but Zn was present in an appreciable amount. This could be explained by the formation of intermediate compound $Zn_xMn_2O_3$ within the cathode which complemented the EDX results [Fig. 12(e)]. A small percentage of S might be due to the stabilization of intermediate compound $Zn_4(OH)_6(SO_4)\cdot 5H_2O$ within the cathode matrix. Fig. 14 shows the valence band spectra of used cathode. A broad peak started from 1.26 to 8.19 eV, indicating the presence of Mn–O bonds in bixbyite. Unlike raw bixbyite [Fig. 5(g)], a sharp peak at 10.42 eV confirmed the presence of a compound like $Zn_xMn_2O_3$. The VBM was calculated to be 1.33 eV.[69]

Table 4 shows a list of specific discharge capacities of prepared Mn-based oxides with respect to the applied current density.[62,63,66,70–83] Several types of Mn-oxides have been prepared for ARZIBs in the literature and some of the Mn-oxides were also doped or coated by conducting materials to increase their capacitive behavior, thereby increasing their preparation cost and complexity. Our explored material showed a comparable result with other materials in terms of the specific discharge

Table 4 List of discharge capacities of Mn-based oxides in ARZIBs

Cathode materials	Applied current density (A g^{-1})	Specific discharge capacity (mA h g^{-1})	References
β-MnO_2	0.10	100	70
δ-MnO_2	0.10	126	70
α-MnO_2	0.02	210	71
α-MnO_2	0.05	255	66
α-MnO_2	0.06	302	72
MnO_2@MgO	0.10	274	73
α-MnO_2/graphene	0.30	362	74
Mn_3O_4@C	0.50	209	75
Mn_2O_3/Mn_3O_4 composite	0.10	122	76
Al-doped MnO_2	0.20	327	77
Mn_3O_4	0.10	221	78
MnO	0.10	330	79
Mn_2O_3	0.10	150	80
α-MnO_2	0.09	290	81
δ-MnO_2	0.10	269	82
Mn_3O_4	0.10	239	83
α-Mn_2O_3	0.10	148	82
α-Mn_2O_3	0.20	137	82
Mn_3O_4	0.10	219	62
Mn_3O_4	0.10	240	63
Mn_2O_3	**0.30**	**255**	**This work**

capacity, while it showed a satisfactory value of specific discharge capacity at higher applied current density (0.3 A g^{-1}). Besides, the preparation process was simpler and cost effective compared with other materials. As a bare compound, the prepared porous Mn_2O_3 micro dice showed acceptable performance as a cathode of ARZIBs compared with other results listed in Table 4.

4. Conclusion

A simple and cost-effective ultrasonic assisted reverse micelle route was used to prepare bixbyite Mn_2O_3 microdice. The prepared Mn_2O_3 showed semiconducting properties, and was used as a cathode in fabricating CR-2032 coin cells of ARZIBs. CV data revealed that the reversible reaction within the cell involved diffusion-controlled (de)intercalation of ions between the anode and cathode by means of high capacitive behavior. It showed relatively higher capacity at lower current density. At 0.3 A g^{-1} current density, the battery showed an initial discharge specific capacity of 252.10 $\pm$ 4.66 mA h g^{-1}, coulombic efficiency of 98.44 $\pm$ 0.27% and a specific capacity retention of 90.35 $\pm$ 0.30% after 1000 cycles.

Data availability

Data are available upon request from the authors.

Conflicts of interest

There are no conflicts of interest to declare.

Acknowledgements

I would like to express my sincere gratitude to the Post-Graduate Laboratory, Department of Chemistry, KUET, Bangladesh, for providing access to their state-of-the-art facilities. I am deeply thankful for the support and resources available, which were instrumental in completing this research.

References

1 C. Wang, Y. Zeng, X. Xiao, S. Wu, G. Zhong, K. Xu and X. Lu, *J. Energy Chem.*, 2020, **43**, 182–187, DOI: 10.1016/j.jechem.2019.08.011.
2 L. Li, H. Xu, Z. Li, B. Zhoong, Z. Lou and L. Wang, *Adv. Mater.*, 2025, **37**, 2414054, DOI: 10.1002/adma.202414054.
3 C. Li, X. Zhang, W. He, G. Xu and R. Sun, *J. Power Sources*, 2020, **449**, 227596, DOI: 10.1016/j.jpowsour.2019.227596.
4 E. J. Hansen and J. Liu, *Front. Energy Res.*, 2021, **8**, 616665, DOI: 10.3389/fenrg.2020.616665.
5 Z. Li, Y. Zheng, L. Liu, L. Li, Z. Lou and L. Wang, *Nat. Electron.*, 2025, 1–10, DOI: 10.1038/s41928-024-01261-6.
6 A. Wang, W. Zhou, A. Huang, M. Chen, Q. Tian and J. Chen, *J. Colloid Interface Sci.*, 2021, **586**, 362–370, DOI: 10.1016/j.jcis.2020.10.099.
7 J. Ming, J. Guo, C. Xia, W. H. Wang and N. Alshareef, *Mater. Sci. Eng., R*, 2019, **135**, 58–84, DOI: 10.1016/j.mser.2018.10.002.
8 J. Shin, J. Lee, Y. Park and J. W. Choi, *Chem. Sci.*, 2020, **11**(8), 2028–2044, DOI: 10.1039/D0SC00022A.
9 S. Chen, F. Tang, T. He, H. Zhang, S. Deng, Y. Li and W. Yan, *Int. J. Photoenergy*, 2019, 1–7, DOI: 10.1155/2019/3792942.
10 A. Huang, W. Zhou, A. Wang, M. Chen, Q. Tian and J. Chen, *J. Energy Chem.*, 2021, **54**, 475–481, DOI: 10.1016/j.jechem.2020.06.041.
11 N. Wang, H. Wan, J. Duan, X. Wang, L. Tao, J. Zhang and H. Wang, *Mater. Today Adv.*, 2021, **11**, 100149, DOI: 10.1016/j.mtadv.2021.100149.
12 X. Guo, J. Zhou, C. Bai, X. Li, G. Fang and S. Liang, *Mater. Today Energy*, 2020, **16**, 100396, DOI: 10.1016/j.mtener.2020.100396.
13 J. Xu, X. Hu, M. A. Alam, G. Muhammad, Y. Lv, M. Wang and W. Xiong, *RSC Adv.*, 2021, **11**(56), 35280–35286, DOI: 10.1039/D1RA06808C.
14 S. Dawadi, A. Gupta, M. Khatri, B. Budhathoki, G. Lamichhane and N. Parajuli, *Bull. Mater. Sci.*, 2020, **43**, 1–10, DOI: 10.1007/s12034-020-02247-8.
15 T. Hatakeyama, N. L. Okamoto and T. Ichitsubo, *J. Solid State Chem.*, 2022, **205**, 122683, DOI: 10.1016/j.jssc.2021.122683.
16 A. Zhang, X. Zhang, H. Zhao, H. Ehrenberg, G. Chen, I. Saadoune and Y. Wang, *J. Colloid Interface Sci.*, 2024, **669**, 723–730, DOI: 10.1016/j.jcis.2024.05.052.
17 H. Shen, B. Liu, Z. Nie, Z. Li, S. Jin, Y. Huang and H. Zhou, *RSC Adv.*, 2021, **11**(24), 14408–14414, DOI: 10.1039/D1RA00346A.
18 L. Narayani, V. J. Angadi, A. Sukhdev, M. Challa, S. Matteppanavar, P. R. Deepthi and M. Pasha, *J. Magn. Magn. Mater.*, 2019, **476**, 268–273, DOI: 10.1016/j.jmmm.2018.12.072.
19 M. Mao, X. Wu, Y. Hu, Q. Yuan, Y. B. He and F. Kang, *J. Energy Chem.*, 2021, **52**, 277–283, DOI: 10.1016/j.jechem.2020.04.061.
20 D. Zhang, J. Cao, X. Zhang, N. Insin, S. Wang, J. Han and Y. Huang, *Adv. Funct. Mater.*, 2021, **31**(14), 2009412, DOI: 10.1002/adfm.202009412.
21 Q. Hou, D. G. Ivey and E. C. S. Inc, *ECS Meeting Abstracts*, 2021, **240**(1), 15, DOI: 10.1149/MA2021-02115mtgabs.
22 K. Cai, S. H. Luo, L. Qian, X. Meng, S. X. Yan, J. Guo and X. Y. Zhou, *J. Power Sources*, 2023, **564**, 232854, DOI: 10.1016/j.jpowsour.2023.232854.
23 G. Zhou, J. Yin, Z. Sun, X. Gao, F. Zhu, P. Zhao and J. Xu, *RSC Adv.*, 2020, **10**(6), 3246–3255, DOI: 10.1039/C9RA08537H.
24 C. Torres-Sanchez and J. R. Corney, *Ultrason. Sonochem.*, 2008, **15**(4), 408–415, DOI: 10.1016/j.ultsonch.2007.05.002.
25 B. Peng, H. Wu, W. Bao, S. Guo, Y. Chen, H. Huang and J. Jow, *Polym. J.*, 2011, **43**(1), 91–96, DOI: 10.1038/pj.2010.95.
26 W. Cai, T. Hu, A. M. Bakry, Z. Zheng, Y. Xiao and Q. Huang, *Ultrason. Sonochem.*, 2018, **42**, 823–831, DOI: 10.1016/j.ultsonch.2017.12.022.
27 S. Lei, Z. Liang, L. Zhou and K. Tang, *Mater. Chem. Phys.*, 2009, **113**(1), 445–450, DOI: 10.1016/j.matchemphys.2008.07.114.

28 S. Lei, K. Tang, Z. Fang, Q. Liu and H. Zheng, *Mater. Lett.*, 2006, **60**(1), 53–56, DOI: **10.1016/j.matlet.2005.07.070**.

29 Z. Zhou, F. Jiang, T. C. Lee and T. Yue, *J. Alloys Compd.*, 2013, **581**, 843–848, DOI: **10.1016/j.jallcom.2013.07.207**.

30 H. Lu, H. Ju, Q. Yang, Z. Li, H. Ren, X. Xin and G. Xu, *CrystEngComm*, 2013, **15**(33), 6511–6517, DOI: **10.1039/C3CE40432C**.

31 Y. Li, Z. Yuan, D. Li, J. Li, Y. Zhang, M. Wang and W. Han, *ACS Nano*, 2024, **18**(6), 4733–4745, DOI: **10.1021/acsnano.3c07977**.

32 J. Liao and Z. Ye, *Batteries*, 2018, **4**(2), 22, DOI: **10.3390/batteries4020022**.

33 S. A. Moon, B. K. Salunke, B. Alkotaini, E. Sathiyamoorthi and B. Kim, *IET Nanobiotechnol.*, 2015, **9**(4), 220–225, DOI: **10.1049/iet-nbt.2014.0051**.

34 V. Sannasi and K. Subbian, *J. Mater. Sci.:Mater. Electron.*, 2020, **31**(19), 17120–17132, DOI: **10.1007/s10854-020-04272-z**.

35 A. K. M. A. Ullah, A. S. M. F. Kibria, M. Aktor, M. N. I. Khan, A. R. M. Tarq and S. H. Firoz, *Water Conserv. Sci. Eng.*, 2017, **1**, 249–256, DOI: **10.1007/s41101-017-0017-3**.

36 B. Wu, G. Zhang, M. Yan, T. Xiong, P. He, L. He and L. Mai, *Small*, 2018, **14**(13), 1703850, DOI: **10.1002/smll.201703850**.

37 C. Martinez de la Torre, J. H. Grossman, A. A. Bobko and M. F. Bennewitz, *PLoS One*, 2020, **15**(9), e0239034, DOI: **10.1371/journal.pone.0239034**.

38 E. A. Tokeser and O. Ozturk, *J. Mater. Sci.: Mater. Electron.*, 2023, **34**(31), 2075, DOI: **10.1007/s10854-023-11402-w**.

39 K. H. Kim, D. K. Lee and Y. H. Choi, *Mater*, 2021, **14**(9), 2338, DOI: **10.3390/ma14092338**.

40 Y. K. Hsu, Y. C. Chen, Y. G. Lin, L. C. Chen and K. H. Chen, *Chem. Commun.*, 2011, **47**(4), 1252–1254, DOI: **10.1039/C0CC03902K**.

41 C. Julien, M. Massot, R. Baddour-Hadjean, S. Franger, S. Bach and J. P. Pereira-Ramos, *Solid State Ionics*, 2003, **159**(3–4), 345–356, DOI: **10.1016/S0167-2738(03)00035-3**.

42 N. Pal, A. Sharma, V. Acharya, N. K. Chourasia, S. Biring and B. N. Pal, *ACS Appl. Electron. Mater.*, 2019, **2**(1), 25–34, DOI: **10.1021/acsaelm.9b00641**.

43 A. A. Audi and P. M. Sherwood, *Surf. Interface Anal.*, 2002, **33**(3), 274–282, DOI: **10.1002/sia.1211**.

44 C. Yun, W. Li, X. Gao, H. Dou, T. Maity, X. Sun and J. L. MacManus-Driscoll, *ACS Appl. Mater. Interfaces*, 2021, **13**(7), 8863–8870, DOI: **10.1021/acsami.1c00607?ref=pdf**.

45 G. Periyasamy, I. M. Patil, B. Kakade, P. Veluswamy, J. Archana, H. Ikeda and K. Annamalai, *J. Mater. Sci.:Mater. Electron.*, 2022, **33**(11), 8644–8654, DOI: **10.1007/s10854-021-06721-9**.

46 Q. Z. Gou, C. Li, X. Q. Zhang, B. Zhang, S. R. Zou, N. Hu and C. X. Lei, *J. Mater. Sci.: Mater. Electron.*, 2018, **29**, 16064–16073, DOI: **10.1007/s10854-018-9695-7**.

47 M. I. Said, A. H. Rageh and F. A. Abdel-Aal, *RSC Adv.*, 2018, **8**(33), 18698–18713, DOI: **10.1039/C8RA02978D**.

48 G. Kumar, N. T. Tonu, P. K. Dhar and M. Mahiuddin, *Pollution*, 2021, **7**(3), 693–707, DOI: **10.22059/poll.2021.320575.1033**.

49 B. Zhang, P. Dong, S. Yuan, Y. Zhang, Y. Zhang and Y. Wang, *Chem Bio Eng.*, 2024, **1**(2), 113–132, DOI: **10.1021/cbe.3c00120?urlappend=%3Fref%3DPDF&jav=VoR&rel=cite-as**.

50 Y. De Luna, A. Alsulaiti, M. I. Ahmad, H. Nimir and N. Bensalah, *Front. Chem.*, 2023, **11**, 1101459, DOI: **10.3389/fchem.2023.1101459**.

51 E. A. Davis and N. Mott, *Philos. Mag.*, 1970, **22**(179), 0903–0922, DOI: **10.1080/14786437008221061**.

52 H. Fritzsche, *Philos. Mag. B*, 1993, **68**(4), 561–572, DOI: **10.1080/13642819308217935**.

53 N. M. Hosny and A. Dahshan, *Mater. Chem. Phys.*, 2012, **137**(2), 637–643, DOI: **10.1016/j.matchemphys.2012.09.068**.

54 D. Zhang, J. Cao, X. Zhang, N. Insin, S. Wang, J. Han and Y. Huang, *Adv. Funct. Mater.*, 2021, **31**(14), 2009412, DOI: **10.1002/adfm.202009412**.

55 K. Lan, Q. Wei, R. Wang, Y. Xia, S. Tan, Y. Wang and D. Zhao, *J. Am. Chem. Soc.*, 2019, **141**(42), 16755–16762, DOI: **10.1021/jacs.9b06962**.

56 G. A. Muller, J. B. Cook, H. S. Kim, S. H. Tolbert and B. Dunn, *Nano Lett.*, 2015, **15**(3), 1911–1917, DOI: **10.1021/nl504764m**.

57 C. Chen, Y. Wen, X. Hu, X. Ji, M. Yan, L. Mai and Y. Huang, *Nat. Commun.*, 2015, **6**(1), 6929, DOI: **10.1038/ncomms7929**.

58 D. Chao, P. Liang, Z. Chen, L. Bai, H. Shen, X. Liu and Z. X. Shen, *ACS Nano*, 2016, **10**(11), 10211–10219, DOI: **10.1021/acsnano.6b05566**.

59 Z. Ye, P. Li, W. Wei, C. Huang, L. Mi, J. Zhang and J. Zhang, *Adv. Sci.*, 2022, **9**(18), 2200067, DOI: **10.1002/advs.202200067**.

60 C. Huang, Q. Wang, G. Tian and D. Zhang, *Mater. Today Phys.*, 2021, **21**, 100518, DOI: **10.1016/j.mtphys.2021.100518**.

61 X. Liu, F. Yang, W. Xu, Y. Zeng, J. He and X. Lu, *Adv. Sci.*, 2020, **7**(21), 2002173, DOI: **10.1002/advs.202002173**.

62 N. T. Tonu, P. Ahamed and M. A. Yousuf, *Ionics*, 2024, 1–15, DOI: **10.1007/s11581-024-05636-9**.

63 N. T. Tonu, P. Ahamed and M. A. Yousuf, *PLoS One*, 2024, **19**(6), e0305611, DOI: **10.1371/journal.pone.0305611**.

64 M. M. Sanad and A. Y. Shenouda, *J. Mater. Sci.: Mater. Electron.*, 2023, **34**(14), 1146, DOI: **10.1007/s10854-023-10555-y**.

65 E. Han, X. Du, P. Yang and Y. Han, *Ionics*, 2018, **24**, 393–401, DOI: **10.1007/s11581-017-2226-3**.

66 O. Ibukun and H. K. Jeong, *New Phys.:Sae Mulli*, 2018, **68**, 185–188, DOI: **10.3938/NPSM.68.185**.

67 A. Morais, J. P. C. Alves, F. A. S. Lima, M. Lira-Cantu and A. F. Nogueira, *J. Photonics Energy*, 2015, **5**(1), 057408, DOI: **10.1117/1.JPE.5.057408**.

68 X. Z. Zhai, J. Qu, S. M. Hao, Y. Q. Jing, W. Chang, J. Wang and Z. Z. Yu, *Nano-Micro Lett.*, 2020, **12**, 1–15, DOI: **10.1007/s40820-020-0397-3**.

69 N. Kamarulzaman, M. F. Kasim and R. Rusdi, *Nanoscale Res. Lett.*, 2015, **10**, 346, DOI: **10.1186/s11671-015-1034-9**.

70 D. Lakshmi and B. Nalini, *J. Solid State Electrochem.*, 2017, **21**, 1027–1034, DOI: **10.1007/s10008-016-3456-4**.

71 E. A. Aboelazm, G. A. Ali, H. Algarni, H. Yin, Y. L. Zhong and K. F. Chong, *J. Phys. Chem. C*, 2018, **122**(23), 12200–12206, DOI: **10.1021/acs.jpcc.8b03306**.

72 L. Wang, X. Cao, L. Xu, J. Chen and J. Zheng, *ACS Sustain. Chem. Eng.*, 2018, **6**(12), 16055–16063, DOI: **10.1021/acssuschemeng.8b02502**.
73 N. Palaniyandy, D. Lakshmi, G. Thenmozhi, S. Kheawhom and N. N. Musyoka, *J. Mater. Sci.*, 2024, **59**(13), 5450–5469, DOI: **10.1007/s10853-024-09373-2**.
74 S. Y. Zhu, Y. F. Yuan, P. F. Du, C. L. Mo, G. C. Cai, B. X. Wang and S. Y. Guo, *Electrochim. Acta*, 2022, **419**, 140396, DOI: **10.1016/j.electacta.2022.140396**.
75 H. Chen, W. Zhou, D. Zhu, Z. Liu, Z. Feng, J. Li and Y. Chen, *J. Alloys Compd.*, 2020, **813**, 151812, DOI: **10.1016/j.jallcom.2019.151812**.
76 J. Yao, Y. Liu, Y. Li, J. Jiang and Q. Zhu, *Mater. Res. Bull.*, 2023, **165**, 112292, DOI: **10.1016/j.materresbull.2023.112292**.
77 Y. Zhao, S. Zhang, Y. Zhang, J. Liang, L. Ren, H. J. Fan and X. Sun, *Energy Environ. Sci.*, 2024, **17**(3), 1279–1290, DOI: **10.1039/D3EE01659E**.
78 L. Wang, X. Cao, L. Xu, J. Chen and J. Zheng, *ACS Sustain. Chem. Eng.*, 2018, **6**(12), 16055–16063, DOI: **10.1021/acssuschemeng.8b02502**.
79 J. Wang, J. G. Wang, H. Liu, Z. You, C. Wei and F. Kang, *J. Power Sources*, 2019, **438**, 226951, DOI: **10.1016/j.jpowsour.2019.226951**.
80 T. Li, J. Tong, S. Liu, J. Liang, G. Dai, W. Sun and A. Sun, *J. Colloid Interface Sci.*, 2024, **656**, 504–512, DOI: **10.1016/j.jcis.2023.11.129**.
81 L. Jiang, Z. Wu, Y. Wang, W. Tian, Z. Yi, C. Cai and L. Hu, *ACS Nano*, 2019, **13**(9), 10376–10385, DOI: **10.1021/acsnano.9b04165**.
82 B. Jiang, C. Xu, C. Wu, L. Dong, J. Li and F. Kang, *Electrochim. Acta*, 2017, **229**, 422–428, DOI: **10.1016/j.electacta.2017.01.163**.
83 L. Gong, Y. Zhang and Z. Li, *J. Electrochem. Soc.*, 2022, **169**(4), 040519, DOI: **10.1149/1945-7111/ac638d**.